REPORT DOCUMENTATION PAGE

Form Approved OMB NO. 0704-0188

1. REPORT DATE (DD-MM-YYYY)	2. REPORT TYPE	3. DATES COVERED (From - To)
09-09-2021	Final Report	1-Jan-2018 - 15-Apr-2021

4. TITLE AND SUBTITLE
Final Report: Coherent-vorticity-Preserving (CvP) Large-Eddy Simulations (LES) of Very-High-Reynolds-Number Vortex Dynamics

5a. CONTRACT NUMBER
W911NF-18-1-0045

5b. GRANT NUMBER

5c. PROGRAM ELEMENT NUMBER
611102

6. AUTHORS

5d. PROJECT NUMBER

5e. TASK NUMBER

5f. WORK UNIT NUMBER

7. PERFORMING ORGANIZATION NAMES AND ADDRESSES
Purdue University
Sponsored Program Services
155 S Grant Street
West Lafayette, IN 47907 -2114

8. PERFORMING ORGANIZATION REPORT NUMBER

9. SPONSORING/MONITORING AGENCY NAME(S) AND ADDRESS (ES)
U.S. Army Research Office
P.O. Box 12211
Research Triangle Park, NC 27709-2211

10. SPONSOR/MONITOR'S ACRONYM(S)
ARO

11. SPONSOR/MONITOR'S REPORT NUMBER(S)
72343-EG-YIP.17

12. DISTRIBUTION AVAILIBILITY STATEMENT
Approved for public release; distribution is unlimited.

13. SUPPLEMENTARY NOTES
The views, opinions and/or findings contained in this report are those of the author(s) and should not contrued as an official Department of the Army position, policy or decision, unless so designated by other documentation.

14. ABSTRACT

15. SUBJECT TERMS

16. SECURITY CLASSIFICATION OF:			17. LIMITATION OF ABSTRACT	15. NUMBER OF PAGES	19a. NAME OF RESPONSIBLE PERSON
a. REPORT	b. ABSTRACT	c. THIS PAGE			Carlo Scalo
UU	UU	UU	UU		19b. TELEPHONE NUMBER 765-494-4600

RPPR Final Report
as of 18-Oct-2021

Agency Code: 21XD

Proposal Number: 72343EGYIP **Agreement Number: W911NF-18-1-0045**
INVESTIGATOR(S):

Name: Carlo Scalo
Email: scalo@purdue.edu
Phone Number: 7654944600
Principal: Y

Organization: **Purdue University**
Address: Sponsored Program Services, West Lafayette, IN 479072114
Country: USA
DUNS Number: 072051394 EIN: 356002041

Report Date: 15-Jul-2021 Date Received: 09-Sep-2021
Final Report for Period Beginning 01-Jan-2018 and Ending 15-Apr-2021

Title: Coherent-vorticity-Preserving (CvP) Large-Eddy Simulations (LES) of Very-High-Reynolds-Number Vortex Dynamics
Begin Performance Period: 01-Jan-2018 **End Performance Period:** 15-Apr-2021
Report Term: 0-Other

Submitted By: Carlo Scalo Email: scalo@purdue.edu
Phone: (765) 494-4600

Distribution Statement: 1-Approved for public release; distribution is unlimited.

STEM Degrees: **STEM Participants:**

Major Goals: The goals of the current proposal are to unravel the physics of very-high-Reynolds-number vortex dynamics by exploiting a new computational technique called coherent-vorticity-preserving (CvP) large-eddy simulation (LES). The CvP-LES technique relies on a very fast evaluation of the local state of spectral broadening based on the application of Kolmogorov's K41 Theory to the filtered enstrophy field. Contrary to popular dynamic models, it only requires one additional filtering operation and very minimal memory overhead, requiring the storage of one extra three-dimensional field.
Three canonical flow setups are targeted:

(1) Single/Double helical vortices: the dynamics of the breakdown to turbulence and the structure of turbulence itself (in the far wake) are investigated spanning a wide range of Reynolds numbers and flow configurations, enabled by the CvP-LES methodology. The goals are to find a dimensionless scaling law to collapse the flow behavior across the entire parameter space and validate against the experiments by Nemes et al. JFM 2015 and Quaranta et al. JFM 2015. This work has been completed and resulted in a JFM paper.

(2) Trefoil knotted vortices: this effort focuses on investigating the effects of the topological complexity of the initial vortical configuration, supported by the experimental results by Kleckner and Irvine, Nature Physics 2013, albeit the latter being limited in terms of Reynolds numbers. One important unsolved question to consider is the physical explanation for the violation of global helicity in this flow.

(3) Vortices under high twist rates exhibit strong instabilities in the form of Writhe and Twist waves. The Purdue group is carrying out investigations of this set up supported by experiments and theoretical analysis carried out by Prof. Irvine

A new software development goal was set for the performance period, which comprises the creation of a high-order adaptive-mesh refinement framework capable of achieving both DNS and scale-adaptive LES. This goal has been met in the current period.

Accomplishments: Goal (1) has been accomplished, and resulted in the following publication:
** Jean-Baptiste Chapelier, Bono Wasistho and Carlo Scalo, Large-Eddy Simulation of temporally developing double helical vortices, Journal of Fluid Mechanics, Vol. 863, pp. 79-113

Goal (2), focused on trefoil vortices, is still in progress. We are currently revising and extending the following paper:

*** Xinran Zhao, Zongxin Yu, Jean-Baptiste Chapelier and Carlo Scalo Direct-Numerical and Large-Eddy Simulation of Trefoil Knotted Vortices Journal of Fluid Mechanics, 2021, Vol 910, A31

Goal (3), numerical simulation of highly perturbed vortex rings, requires the development of an adaptive-mesh-refinement code which is now complete. A brand new paper has been published in J. Fluid Mechanics as a result:
*** Xinran Zhao and Carlo Scalo, Helicity dynamics in reconnection events of topologically complex vortex flows Journal of Fluid Mechanics, 2021, Vol 920, A3

This paper contains a key analytical contribution, unraveling the fundamental mechanisms linking circulation transfer and helicity change.

Training Opportunities: Nothing to Report

Results Dissemination: Due to the pandemic, there are no conference papers to report during this period. However, numerous high-caliber journal publications resulted from this grant.

Honors and Awards: Nothing to Report

Protocol Activity Status:

Technology Transfer: Nothing to Report

PARTICIPANTS:

Participant Type: Faculty
Participant: William Irvine
Person Months Worked: 12.00 **Funding Support:**
Project Contribution:
National Academy Member: N

ARTICLES:

Publication Type: Journal Article Peer Reviewed: Y **Publication Status:** 1-Published
Journal: Journal of Computational Physics
Publication Identifier Type: DOI Publication Identifier: 10.1016/j.jcp.2018.01.012
Volume: 359 Issue: n/a First Page #: 164
Date Submitted: 10/3/18 12:00AM Date Published: 4/1/18 4:00AM
Publication Location: West Lafayette, IN
Article Title: A Coherent vorticity preserving eddy-viscosity correction for Large-Eddy Simulation
Authors: J.-B. Chapelier, B. Wasistho, C. Scalo
Keywords: Large-Eddy Simulation;Dynamic models; Coherent vortices; Enstrophy; Turbulence sensor
Abstract: This paper introduces a new approach to Large-Eddy Simulation (LES) where subgrid- scale (SGS) dissipation is applied proportionally to the degree of local spectral broadening, hence mitigated or deactivated in regions dominated by large-scale and/or laminar vortical motion. The proposed coherent-vorticity preserving (CvP) LES methodology is based on the evaluation of the ratio of the test-filtered to resolved (or grid-filtered) enstrophy, sigma. Values of sigma close to 1 indicate low sub-test-filter turbulent activity, justifying local deactivation of the SGS dissipation. The intensity of the SGS dissipation is progressively increased for sigma < 1 which corresponds to a small-scale spectral broadening. The SGS dissipation is then fully activated in developed turbulence, sigma = sigma_eq, where the value sigma_eq is derived assuming a Kolmogorov spectrum. The proposed approach can be applied to any eddy-viscosity model, is algorithmically simple and computationally inexpensive.
Distribution Statement: 3-Distribution authorized to U.S. Government Agencies and their contractors
Acknowledged Federal Support: **Y**

RPPR Final Report
as of 18-Oct-2021

Publication Type: Journal Article Peer Reviewed: Y **Publication Status:** 1-Published
Journal: Journal of Fluid Mechanics
Publication Identifier Type: DOI Publication Identifier: 10.1017/jfm.2018.910
Volume: 863 Issue: First Page #: 79
Date Submitted: 5/10/19 12:00AM Date Published:
Publication Location:
Article Title: Large-Eddy Simulation of Temporally Developing Double Helical Vortices
Authors: J.-B. Chapelier, B. Wasistho and C. Scalo
Keywords: Helical vortex; Vortex dynamics; Mutual inductance; Large-Eddy Simulation; Turbulence; Anisotropy
Abstract: This paper investigates the transient regime and turbulent wake characteristics of temporally developing double helical vortices via high-fidelity large-eddy simulation (LES) for circulation Reynolds numbers in the range Re? =7000–70000, vortex-core radii between rc = 0.06R and 0.2R and helical pitches in the range h = 0.36R–0.61R, where R is the initial helix radius. The present study achieves three objectives: (i) assess the influence of Re?, rc and h on the growth rates of the helical vortex instability driven by mutual inductance; (ii) characterize the type of vortex reconnection events that appear during transition; (iii) study the characteristics of turbulence in the far wake, and in particular quantify the anisotropy in the flow. The initial transient dynamics is conveniently described in terms of the non-dimensional time t? = t? /h2, yielding the dimensionless growth rate of ?? ? 20 and collapsing of all the LES data for a given rc/h ratio.
Distribution Statement: 3-Distribution authorized to U.S. Government Agencies and their contractors
Acknowledged Federal Support: **Y**

Publication Type: Journal Article Peer Reviewed: Y **Publication Status:** 1-Published
Journal: Journal of Fluid Mechanics
Publication Identifier Type: Publication Identifier:
Volume: Issue: First Page #:
Date Submitted: 7/30/21 12:00AM Date Published:
Publication Location:
Article Title: Large-Eddy Simulation of Trefoil Knotted Vortices
Authors: Zongxin Yu, Jean-Baptiste Chapelier, Carlo Scalo
Keywords: coherent vorticity, knotted vortices, large-eddy simulation
Abstract: This paper proposes a study of vortex reconnection mechanisms at high Reynolds numbers (up to Re_\Gamma = 2 × 105) by the means of high-fidelity Large-Eddy simulations (LES) of a trefoil knot-shaped vortex, inspired by the experiments of Kleckner & Irvine (2013). The LES computations are first validated against experiments, with the size of computation domain selected according to two point velocity correlations, and the methodology is found to capture correctly the vortex entanglement process as well as the subsequent separation of the main vortex in two distinct structures - a small and a large vortex - with different self-advection speeds. The advection velocity of the vortex before reconnection is found to be independent of the Reynolds number, while after separation the small vortex propagates around 2.5 times faster than the large oscillatory structure which carries an important amount of vorticity. The details of the ”bridging” process are characterized during the reconnection.
Distribution Statement: 3-Distribution authorized to U.S. Government Agencies and their contractors
Acknowledged Federal Support: **Y**

RPPR Final Report
as of 18-Oct-2021

Publication Type: Journal Article Peer Reviewed: Y **Publication Status:** 1-Published
Journal: Journal of Fluid Mechanics
Publication Identifier Type: Publication Identifier: 10.1017/jfm.2020.943
Volume: 910 Issue: A31 First Page #: 1
Date Submitted: 6/16/21 12:00AM Date Published:
Publication Location:
Article Title: Direct-Numerical and Large-Eddy Simulation of Trefoil Knotted Vortices
Authors: Xinran Zhao, Zongxin Yu, Jean-Baptiste Chapelier, and Carlo Scalo
Keywords: knotted vortex, adaptive mesh refinement, large-eddy simulation, helicity
Abstract: This paper investigates pre- and post-reconnection dynamics of a trefoil knotted vortex for circulation-based Reynolds numbers up to Re = 2 × 105 by means of direct numerical simulation (DNS) and coherent-vorticity preserving (CvP) large-eddy simulations (LES). The complete flow evolution is simulated, including the turbulence production upon reconnection, subsequent separation into a smaller and a larger vortex ring, and, finally, the formation of Kelvin waves. The self-advection velocity of the trefoil before reconnection is found to scale with inviscid parameters, whereas vortex propagation speeds after separation retain viscous effects, more prominent for the smaller vortex ring; the larger one is responsible for the bulk of the helicity and enstrophy generation and transport after reconnection. The volume-averaged helicity is conserved only before reconnection, which is followed by a production of helicity due to small-scale vortical events during the bridging process.
Distribution Statement: 2-Distribution Limited to U.S. Government agencies only; report contains proprietary info
Acknowledged Federal Support: **Y**

Publication Type: Journal Article Peer Reviewed: Y **Publication Status:** 1-Published
Journal: Journal of Fluid Mechanics
Publication Identifier Type: DOI Publication Identifier: 10.1017/jfm.2021.455
Volume: 920 Issue: A30 First Page #:
Date Submitted: 6/16/21 12:00AM Date Published:
Publication Location:
Article Title: Helicity Dynamics in Reconnection Events of Topologically Complex Vortex Flows
Authors: Xinran Zhao, Carlo Scalo
Keywords: vortex dynamics, helicity, adaptive-mesh-refinement
Abstract: In this paper, we address the question of whether total helicity is conserved through viscous reconnection events in topologically complex vortex flows. To answer this question, we performed direct numerical simulations (DNS) focused on two complex vortex flow problems: (1) a trefoil knot and (2) a two-ring link, both simulated for various vortex core radii. The DNS framework relies on a block-structured adaptive mesh refinement (AMR) technique. A third simulation of a colliding pair of unlinked vortex rings, which exhibit no total helicity change, is also performed to serve as a reference case. The results show that a well-defined total helicity jump occurs during the unknotting/unlinking events of cases (1) and (2), which arises from the annihilation of the local helicity density content in the reconnection regions. Changes in total helicity become steeper as thinner core radii are considered for both cases (1) and (2). Finally, an analytical derivation is provided.
Distribution Statement: 2-Distribution Limited to U.S. Government agencies only; report contains proprietary info
Acknowledged Federal Support: **Y**

CONFERENCE PAPERS:

Publication Type: Conference Paper or Presentation **Publication Status:** 1-Published
Conference Name: 2018 AIAA Aerospace Sciences Meeting
Date Received: 03-Oct-2018 Conference Date: 08-Jan-2018 Date Published: 12-Jan-2018
Conference Location: Kissimmee, Florida
Paper Title: Coherent-vorticity Preserving Large-Eddy Simulation of trefoil knotted vortices
Authors: Zongxin Yu, Jean-Baptiste Chapelier, Carlo Scalo
Acknowledged Federal Support: **Y**

RPPR Final Report
as of 18-Oct-2021

Publication Type: Conference Paper or Presentation **Publication Status:** 1-Published
Conference Name: 2018 Fluid Dynamics Conference
Date Received: 03-Oct-2018 Conference Date: 25-Jun-2018 Date Published: 29-Jun-2018
Conference Location: Atlanta, Georgia
Paper Title: Coherent-vorticity Preserving Large-Eddy Simulation of vortex rings under large perturbations
Authors: Z. Yu, J.-B. Chapelier, C. Scalo
Acknowledged Federal Support: **Y**

Publication Type: Conference Paper or Presentation **Publication Status:** 1-Published
Conference Name: AIAA -- SciTech
Date Received: Conference Date: 06-Jan-2020 Date Published: 13-Jan-2020
Conference Location: Orlando, FL
Paper Title: A compact-finite-difference-based numerical framework for adaptive-grid-refinement simulations of vortex-dominated flows
Authors: Xinran Zhao, Carlo Scalo
Acknowledged Federal Support: **Y**

WEBSITES:

URL: https://engineering.purdue.edu/~scalo/menu/projects/turbulence_modeling.html
Date Received: 03-Oct-2018
Title: Dr. Scalo's Compressible Flow and Acoustics Lab
Description: Another page from Dr. Scalo's website advertising work carried out under this ARO-YIP grant.
URL: https://engineering.purdue.edu/~scalo/menu/projects/vortex_dynamics.html
Date Received: 03-Oct-2018
Title: Dr. Scalo's Compressible Flow and Acoustics Lab
Description: Page from Dr. Scalo's Lab advertising work funded by this ARO-YIP.
URL: https://engineering.purdue.edu/~scalo/menu/projects/turbulence_modeling.html
Date Received: 03-Oct-2018
Title: Dr. Scalo's Compressible Flow and Acoustics Lab
Description: Another page from Dr. Scalo's website advertising work carried out under this ARO-YIP grant.

Partners

,

I certify that the information in the report is complete and accurate:
Signature: Carlo Scalo
Signature Date: 9/9/21 7:38PM

FY18 ARO-YIP Final Report:

"Coherent-vorticity-Preserving (CvP) Large-Eddy Simulations of Very-High-Reynolds-Number Vortex Dynamics"

prepared by:

Dr. Xinran Zhao, Dr. Jean-Baptiste Chapelier, Mr. Nicola M. Lucarelli
Prof. Carlo Scalo
School of Mechanical Engineering, Purdue University

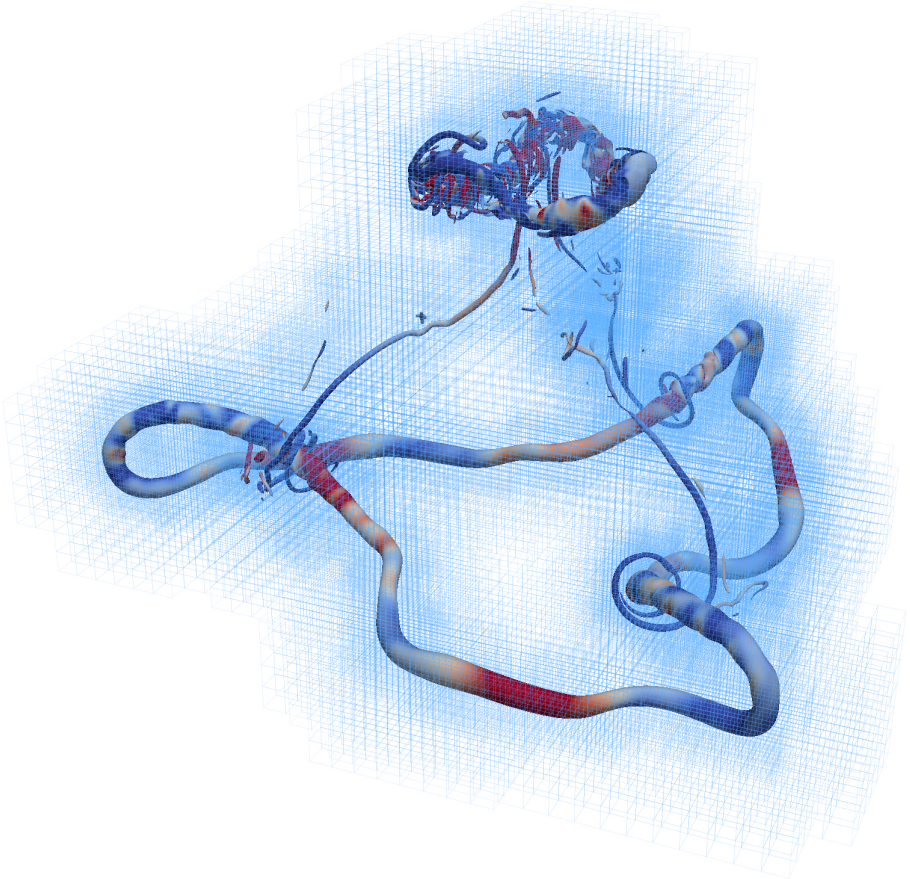

Large-Scale Adaptive-Mesh-Refinement (AMR) Direct-Numerical-Simulation of a trefoil vortex at circulation Reynolds number $Re_\Gamma = 6000$. *Iso-surfaces are coloured by helicity density.*

Grant no. W911NF-18-1-0045
Dr. Matthew Munson
Program Manager, Fluid Dynamics
Mechanical Sciences Division
Engineering Sciences Directorate
U.S. Army Research Office

Objectives of ARO Grant no. W911NF-18-1-0045

Grant Objectives At Glance

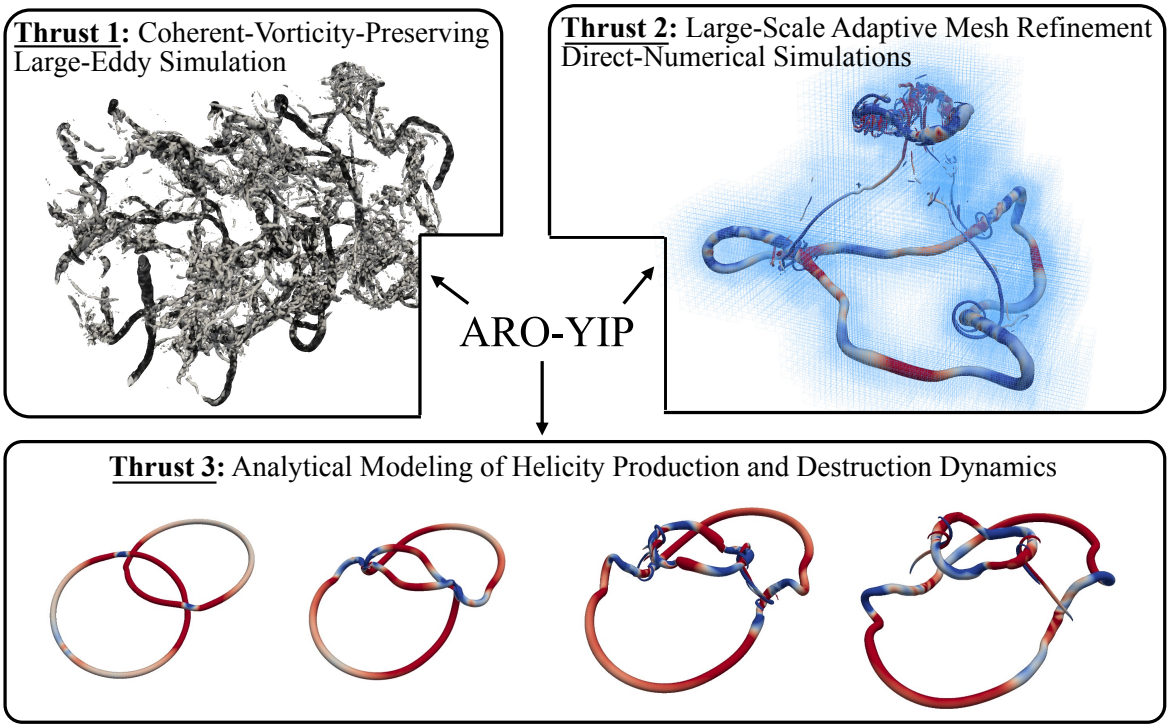

Figure 1: Overview of the three main thrusts of this ARO-YIP effort in vortex dynamics.

The main thrusts of this ARO-YIP effort are the development of advanced large-eddy simulation techniques for vortex-dominated turbulent flows at very high circulation Reynolds numbers (**Thrust 1**), an adaptive-mesh-refinement technique for large-scale direct-numerical-simulations of topologically complex vortices (**Thrust 2**), and analytical modeling of helicity annihilation dynamics (**Thrust 3**).

In the following, we outline the fundamental fluid dynamic questions tackled by this grant, and the resulting achievements, successes and challenges encountered along the path.

Fundamental Fluid Dynamic Questions Addressed

The complexity of the flows being tackled naturally yields the following fundamental questions to be addressed. In (**Thrust 1**): Can a Large-Eddy Simulation technique allows us to reproduce very high Reynolds number experimental results at a reasonable cost? What is the mathematical form of the subgrid-scale contribution to helicity production and destruction and can LES capture it? In (**Thrust 2**): What are the dynamics of the turbulent bursting phenomenon occurring upon vortex entanglement and reconnection, and does their dependency on the circulation Reynolds number vanish in the inviscid limit? Finally, in (**Thrust 2**): what are the fundamental mechanisms underlying helicity production and dissipation? Can they be analytically related to circulation transfer?

Relevance to the US Army

This ARO effort has allowed us to execute very-high-Reynolds-number LES simulations of transitional and turbulent vortex dominated flows of interest to the US Army at a much lower cost and higher accuracy than before. This grant has established a new form of LES methodology, which already provides computational savings up to 40% compared to SOTA Dynamics LES models [4]. The PI commits to assisting in the implementation of CvP-LES models in similar flow prediction codes available to the US Army. The first successful application of such LES technique has been to double helical vortices, representative of tip-to-tip vortex interactions, and inform the design of coaxial rotors (see figure 2), at flow conditions relevant to the Army [6]; New discoveries into reconnection and entanglement events in knotted vortices inform modeling of interactions between coherent vorticity emanating from different rotating lifting elements of a helicopter (e.g. vorticity from main blades interacting with stabilizer blades); Another important aspect of the work provides analytical modeling support for tackles the study of turbulent wakes such as the ones emanating from a leading blade onto a following blade, informing the design of multi-blade rotors and single-blade airfoils.

Figure 2: AVX is currently refining its proposal for the U.S. Army Future Vertical Lift (FVL) aircraft, developing a Coaxial Compound Helicopter concept shown in figure. Photo courtesy of `http://www.avxaircraft.com`.

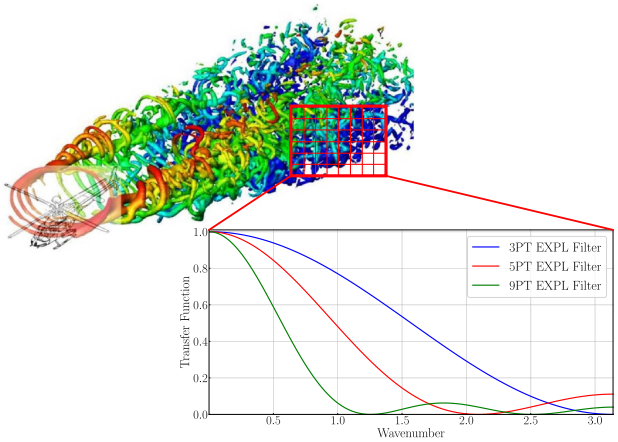

Figure 3: Highly-turbulent vortex dynamics in rotor-wake, with a visualization of where CvP-LES technology can be applied.

The state-of-the-art technology, CvP-LES, developed under this grant is ready for implementation into the various Department of Defense NAVAIR codes such as Kestrel or Helios from the AV-CREATE software suite. The addition of CvP to these robust codes would allow for more accurate calculations done in the off-body region where large-scale turbulent dynamics are of great influence. Using the structured off-body grid, high-fidelity calculations predicting the temporal evolution and interactions of rotorcraft wake could be completed at a much lower cost using CvP-LES technology. Along with the vortex-blade interactions within one flight vehicle, low-cost high-fidelity simulations of the rotorblade wake are critical when analyzing situations involving closely trailing flight vehicles, such as compact take-off and landing areas.

Summary of Publications

This section summarizes the journal articles and conference proceedings published under the support of this ARO Grant no. W911NF-18-1-0045 in chronological order.

#1: Coherent-vorticity Preserving (CvP) Large-Eddy Simulation (LES)

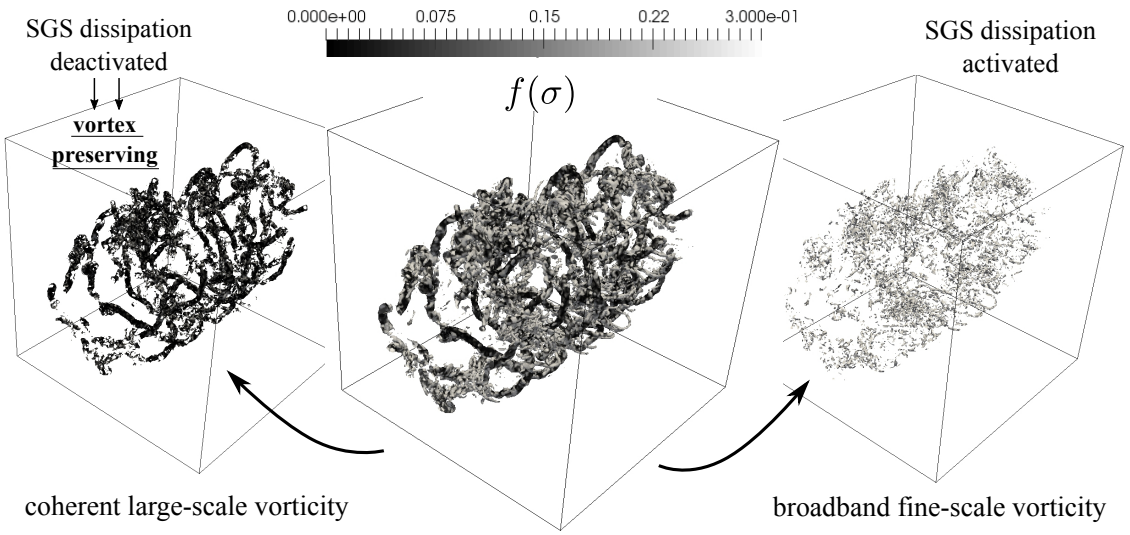

Figure 4: CvP-LES of a double helical vortex breakdown (see Thrust 1) on a 128^3 grid. Decomposition into coherent-vortex-dominated regions (left, in black) and broadband small-scale turbulence (right, in white).

We have introduced a new approach to Large-Eddy Simulation (LES) where subgrid-scale (SGS) dissipation is applied proportionally to the degree of local spectral broadening, hence mitigated or deactivated in regions dominated by large-scale and/or laminar vortical motion. The proposed coherent-vorticity preserving (CvP) LES methodology is based on the evaluation of the ratio of the test-filtered to resolved (or grid-filtered) enstrophy, σ. Values of σ close to 1 indicate low sub-test-filter turbulent activity, justifying local deactivation of the SGS dissipation. The intensity of the SGS dissipation is progressively increased for $\sigma <$ 1 which corresponds to a small-scale spectral broadening. The SGS dissipation is then fully activated in developed turbulence characterized by $\sigma \leq \sigma_{\text{eq}}$, where the value eq is derived assuming a Kolmogorov spectrum. LES of Taylor–Green vortex breakdown demonstrates that the CvP methodology improves the performance of traditional, non-dynamic dissipative SGS models, capturing the peak of total turbulent kinetic energy dissipation during transition with the same accuracy as Germano's dynamic procedure albeit at more than twice the computational overhead.

Chapelier, Wasistho, & Scalo (2018). *A coherent vorticity preserving eddy-viscosity correction for large-eddy simulation.* **Journal of Computational Physics**, 359, 164-182.

#2: CvP-LES of Temporally Developing Double-Helical Vortices

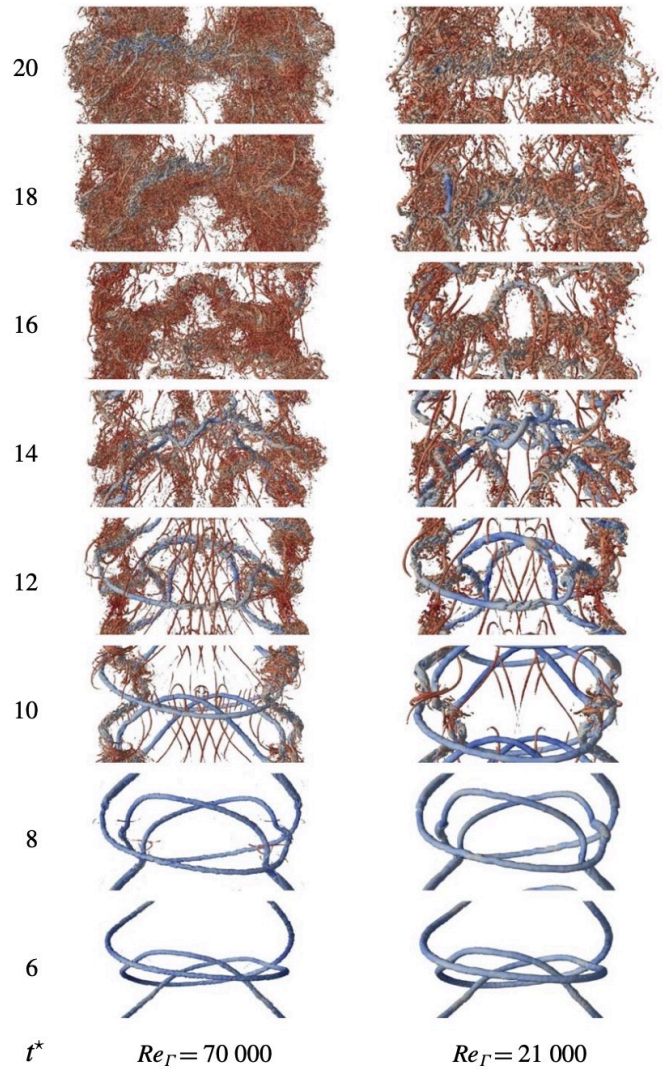

Figure 5: Transition to turbulence of a double helical vortex, Q-isosurfaces colored by pressure.

This paper investigated the transient regime and turbulent wake characteristics of temporally developing double helical vortices via high-fidelity large-eddy simulation (LES) for circulation Reynolds numbers in the range Re_Γ =7000–70000, for various vortex radii and helical pitches.

Three objectives have been achieved:

(i) assess the influence of Re_Γ, vortex core radius r_c, and pitch h on the growth rates of the helical vortex instability and resulting turbulence;

(ii) classify the type of vortex reconnection events during transition;

(iii) characterize the degree of isotropy and memory of the far wake turbulence.

The initial transient dynamics is conveniently described in terms of the non-dimensional time $t^* = t\Gamma/h^2$, yielding the dimensionless growth rate of $\alpha \sim 20$ and collapsing of all the LES data for a given r_c/h ratio. The vortex-core displacement growth rate is found to be Reynolds-number independent, and decreases for larger r_c/h ratios.

Several vortex reconnection events are identified during the transition, mostly initiated by the leap frogging of helical vortices. This phenomenon causes the entanglement of orthogonal vortex filaments, leading to their separation, followed by the creation of elongated threads in the axial direction. The study of integral length scales shows the presence of a strong large-scale anisotropy, retaining the memory of the initial helical pitch h, in particular for the integral scale in the axial direction. The large-scale anisotropy is propagated through the inertial and dissipative ranges, determined from the computation of the moments of velocity gradients in the three directions.

Chapelier, Wasistho, & Scalo (2019). *Large-eddy simulation of temporally developing double helical vortices.* **Journal of Fluid Mechanics**, 863, 79-113.

#3: Adaptive-Grid-Refinement Simulations of Vortex-Dominated Flows

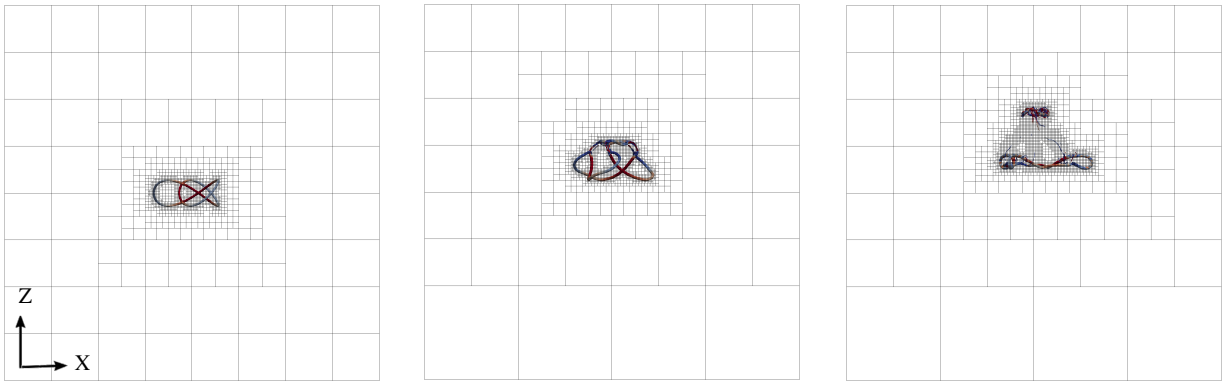

Figure 6: Grid following the vortex transport with AMR, in the DNS simulation of trefoil knotted vortex at Re_Γ = 6000 at three different time steps.

This paper presents an adaptive mesh refinement method for DNS simulating turbulent flows, with focus on simulating vortex dynamics problems. The compressible Navier-Stokes equations are solved on the multi-block computational domain with compact-finite-difference scheme. Staggered arrangement for variables are used which has shown superior advantage in robustness and accuracy for turbulent flow simulations. With the combination of high-order interpolation and high-order compact difference operator, an overall 4th-order accuracy in space can be achieved. The refinement test function is given by a sensor based on the gradient of vorticity. Test cases on vortex dynamics problems have shown that this sensor is capable of capturing and refining the location where the strain-rate is high and turbulent breakdown occurs. Future work includes DNS simulations on a topologically complicated knotted vortex reconnection problems at high Reynolds number.

Zhao & Scalo (2020). *A compact-finite-difference-based numerical framework for adaptive-grid-refinement simulations of vortex-dominated flows.* **AIAA-Scitech** p. 0810.

#4: Direct-Numerical and Large-Eddy Simulation of Knotted Vortices

This paper investigates pre- and post-reconnection dynamics of an unperturbed trefoil knotted vortex for circulation-based Reynolds numbers Re_Γ = 2,000 and 6,000 by means of direct numerical simulations based on an adaptive mesh refinement framework. Companion coherent-vorticity preserving large-eddy simulations are also carried out on a uniform Cartesian grid. The complete vortex structure and flow evolution are simulated, including reconnection and subsequent separation into a smaller and a larger vortex ring, and the resulting helicity dynamics. The self-advection velocity before reconnection is found to scale with inviscid parameters. The reconnection process, however, occurs earlier (and more rapidly) in the higher Reynolds number case due to higher induced velocities associated with a thinner vortex core. The vortex propagation velocities after reconnection and separation

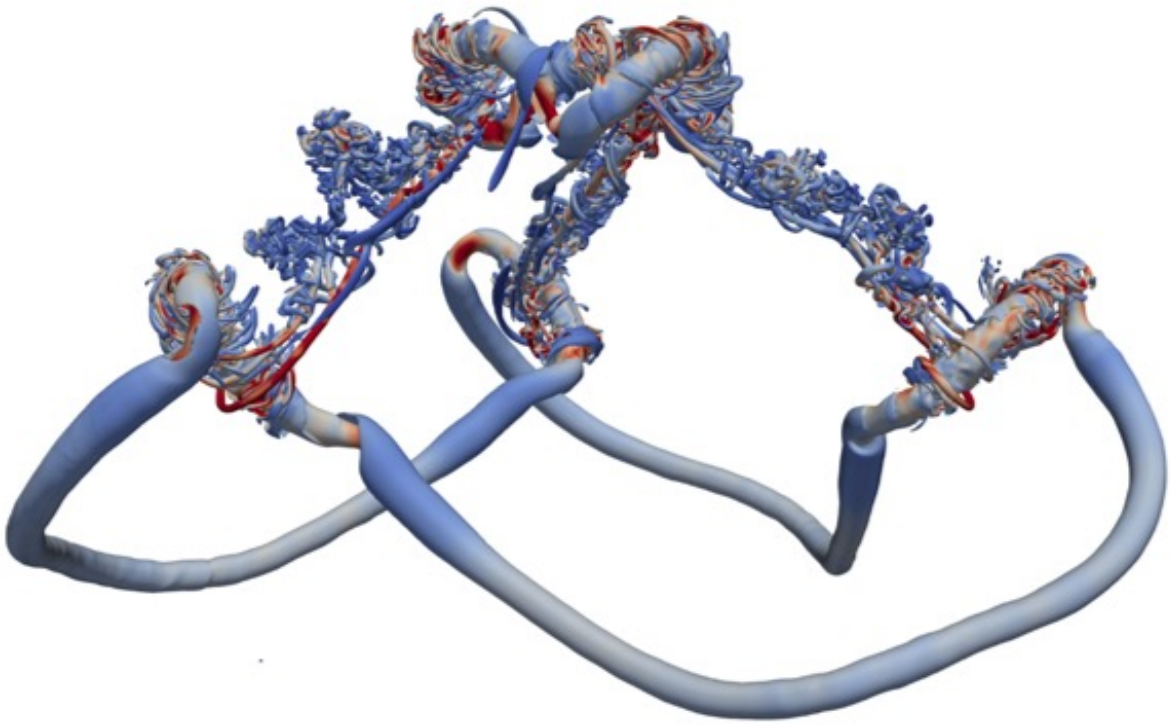

Figure 7: Fully resolved coherent and small-scale vortex structures at a moment during the vortex reconnection of a trefoil knotted vortex at high Reynolds number with the Adaptive Mesh Refinement package VAMPIRE. The simulation is simulated with 1.16 billion degrees of freedom, and more than 2 million CPU-hours on one of the newest DoD supercomputing clusters.

are also affected by viscous effects, more prominently for the smaller vortex ring; the larger one is shown to carry the bulk of the helicity and enstrophy after reconnection. The domain integrated, or total helicity, $H(t)$, does not significantly change up until reconnection, at which point it varies abruptly due to the rapid dissipation of helicity caused by super-helicity hotspots localized at the reconnection sites. The total helicity dissipation rate predicted by the large-eddy simulation agrees reasonably well with the direct numerical simulation results, with a significant contribution from the modelled subgrid-scale stresses. On the other hand, variations in the vortex centreline helicity, $H_C(t)$, and the vortex-tube-integrated helicity $H_V(t)$ are less sensitive to the reconnection process. Periodic vortex bursting events are also observed and are shown to be due to converging axial flow velocities in the detached vortex rings at later stages of evolution.

Zhao, Yu, Chapelier, & Scalo (2021). *Direct numerical and large-eddy simulation of trefoil knotted vortices.* **Journal of Fluid Mechanics**, Vol 910, A31

#5: Modeling of Helicity Jumps in Topologically Complex Vortex Flows

In this paper, we address the question of whether total helicity is conserved through viscous reconnection events in topologically complex vortex flows. To answer this question, we performed direct numerical simulations (DNS) focused on two complex vortex flow problems: (1) a trefoil knot and (2) a two-ring link, both simulated for various vortex core radii.

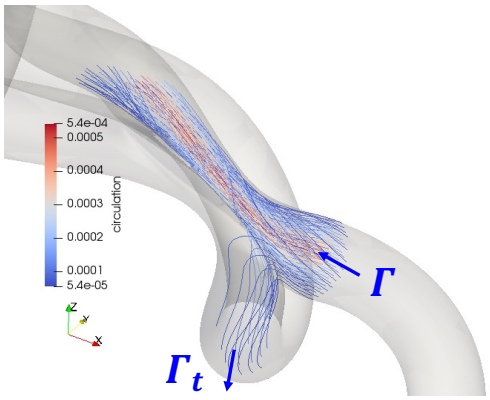

Figure 8: Vorticity transfer during selected simulation for a trefoil knot with $r_c = 2$ mm at $t\Gamma/R^2 = 2.792$, and the vortex tube is visualized by the vorticity isosurface $\omega R^2/\Gamma = 5.7$.

The DNS framework relies on a block-structured adaptive mesh refinement (AMR) technique. A third simulation of a colliding pair of unlinked vortex rings, which exhibit no total helicity change, is also performed to serve as a reference case. The results show that a well-defined total helicity jump occurs during the unknotting/unlinking events of cases (1) and (2), which arises from the annihilation of the local helicity density content in the reconnection regions. Changes in total helicity become steeper as thinner core radii are considered for both cases (1) and (2). Finally, an analytical derivation based on the reconnection of two infinitesimal anti-parallel vortex filaments is provided that quantitatively links helicity annihilation and viscous circulation transfer processes, which unveils the fundamental hydrodynamic mechanisms responsible for production/destruction of total helicity during reconnection events. The resulting model is successful in predicting the previously mysterious helicity 'jump' discovered with the DNS and LES simulation of the knotted vortex (Figure 9).

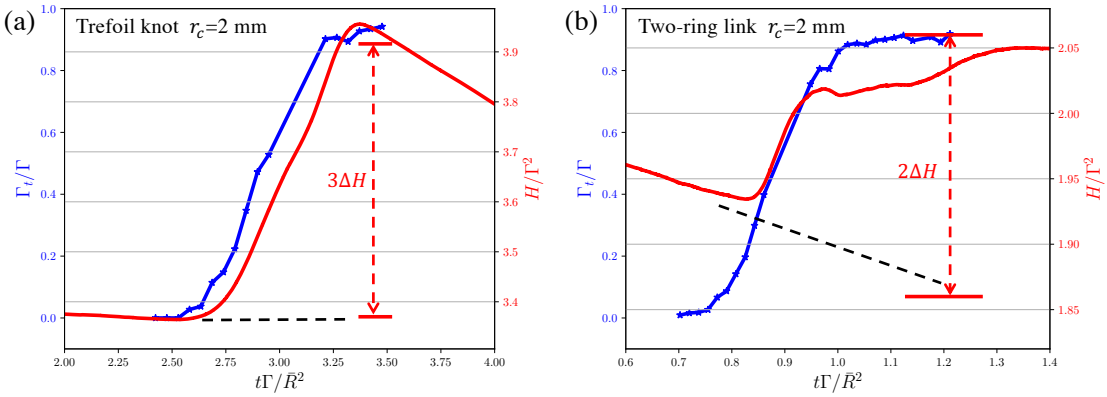

Figure 9: The circulation transfer (blue) of trefoil knot (a) and two-ring link (b) for r_c = 2 mm, compares to the time series of helicity change (red), with dashed lines remarking ΔH multiplied by the number of reconnection sites.

Zhao & Scalo (2021). *Helicity dynamics in reconnection events of topologically complex vortex flows.* **Journal of Fluid Mechanics**, 920.

Accomplishment 1: Coherent-vorticity-Preserving (CvP) Large-Eddy Simulation (LES)

Methodology: Enstrophy-based Modulation of Turbulent Eddy Viscosity

The new CvP-LES technique by Chapelier & Scalo, AIAA 2017-4168 [7] deactivates subgrid-scale (SGS) dissipation in areas of large-scale vorticity, preserving coherent structures, while restoring it in fully turbulent regions (figure 4). CvP-LES enables the investigation of very high Reynolds number and topologically complex vortex- dominated flow problems (described in the 'Statement of Objectives' section), which are (1) inaccessible by DNS, or (2) not predictable with the same fidelity by other state-of-the-art LES methods at the same cost. For example, CvP-LES calculations shown in figure 4 are carried out with only 3 grid points per vortex core (128^3 grid) but nonetheless matching experimentally observed growth rates (figure 14). A DNS of the same flow requires approximately 1000^3 points. An LES simulation at 128^3 with a classic Smagorinsky model does not predict transition to turbulence, which is, on the other hand, captured by a Dynamic-LES albeit overestimating the decay rate of the large structures compared to CvP-LES.

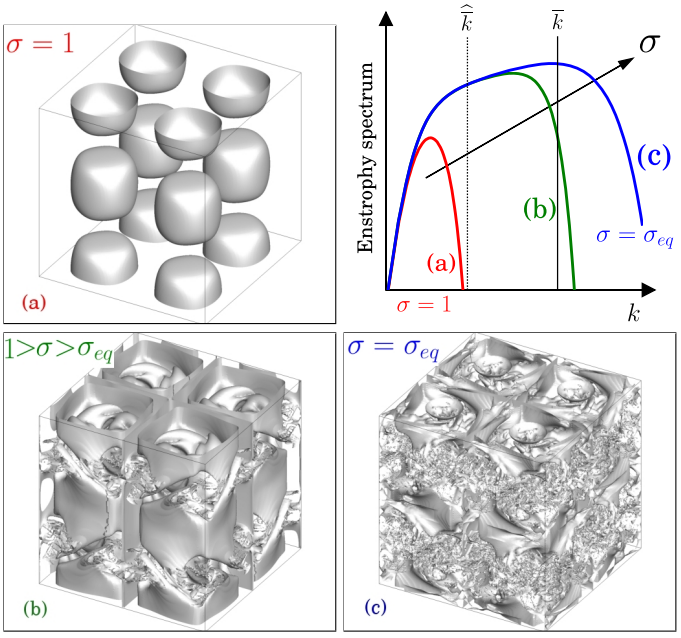

Figure 10: Evolution of ratio $\sigma = \widehat{\overline{\xi}}/\overline{\xi}$, see Eqn. (1), in a CvP-LES of TGV breakdown.

CvP-LES is based on the evaluation of the local ratio $\sigma(\mathbf{x})$ of the instantaneous test-filtered, $\widehat{\overline{\xi}}$, to resolved (or grid-filtered), $\overline{\xi}$, enstrophy, i.e.

$$\sigma = \widehat{\overline{\xi}}/\overline{\xi}; \quad \xi = \boldsymbol{\omega}\cdot\boldsymbol{\omega}/2; \qquad (1)$$

where $\boldsymbol{\omega} = \boldsymbol{\nabla}\times\boldsymbol{u}$ is the vorticity field. An eddy-viscosity correction function $f(\sigma)$ (see figure 12) is then introduced

$$\mu_{SGS}^{(\mathrm{CvP})} = f(\sigma(\mathbf{x}))\,\mu_{SGS} \qquad (2)$$

with bounds $f(\sigma = 1) = 0$ and $f(\sigma < \sigma_{eq}) = 1.0$ since $\sigma = 1$ corresponds to narrowband, large-scale vortical regions where SGS dissipation should not be active (figure 10a); whereas σ_{eq} is the theoretical value based on Kolmogorov's fully developed turbulent model spectrum (figure 10c), requiring SGS dissipation. **The CvP-LES approach hence removes unnecessary SGS dissipation, can be applied to any eddy-viscosity model, is algorithmically simple, computationally less expensive than other dynamic models and extendable to non-structured grids.**

One expected shortcoming of traditional LES modeling approaches is their tendency to introduce excess SGS dissipation in transitional or locally low-Reynolds-number regions, where the flow is well resolved, or, similarly, impacts the evolution of the large coherent vortices, which may be on the verge of break-up and transition to turbulence or coexist

within finer-scale broadband vorticity. CvP-LES remedies this issue as explained in the 'Overview of CvP-LES' section above and demonstrated in the following.

The plain Smagorinsky model [53], in fact, attenuates velocity gradients at all scales of the flow, resulting in the unphysical damping of coherent laminar vortices or suppression transitional regions. In TGV breakdown simulations the same issue is observed with Vreman [58] and Structure Function (SF) [37] models (figure 11a).

The so-called Dynamic procedure [15] aims at correcting the overly dissipative nature of SGS models by determing dynamically the subgrid model parameter, mitigating SGS dissipation for transitional or inhomogeneous flows [15, 16, 29, 36, 42]. **Such approach, however, sensibly increases the cost (table 1), memory requirements and complexity of the implementation.** This is due to the test-filtering of many auxiliary tensors and the need for averaging of the dynamic parameter along directions of statistical homogeneity, or flow path trajectories, to obtain stable computations. The averaging of the dynamic parameter neglects spatial variations of the state of turbulence, which constitutes a first-order error in flows simultaneously presenting both transitional and fully developed turbulence regions, such as the double helical vortex shown in the cover page.

This shortcoming is avoided in the context of the CvP-LES methodology, which enables spatial variations of the dynamic parameter, allowing to effectively discriminate transitional/laminar from broadband turbulent regions. Surprisingly, the spatially averaged dynamic parameter from the Dynamic-LES based on Germano's identity [15] is found to exhibit oscillations not present in the CvP-LES methodology (figure 11b).

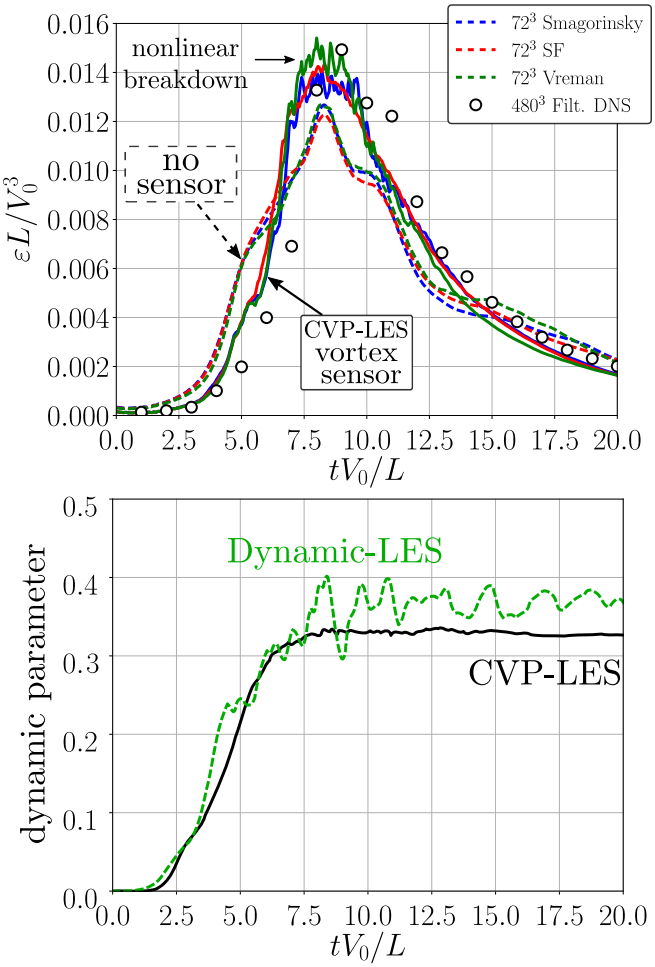

Figure 11: Turbulent dissipation from TGV at Re=5000 using three classic SGS models with (solid line) and without (dashed line) CvP sensor (a); Dynamic parameter from CvP-LES compared to the Dynamic-LES based on Germano's identity (b).

CvP-LES allows for an accurate representation of the evolution of turbulent dissipation as the sensor function is able to reduce the SGS contribution in the early stages of transition, improving the performance of any SGS model (figure 11).

Model	CPU Time	Overhead	Auxiliary 3D Arrays	Filtering operations
No SGS model	t_{ref}	-	0	0
Smagorinsky	$1.134t_{ref}$	+13.4	6	0
CvP-LES + Smag. [7]	$1.151t_{ref}$	+15.1	8	1
Dynamic-LES [15]	$1.404t_{ref}$	+40.4	18	23

Table 1: Computational cost comparison among different LES methods in TGV simulations.

In summary, the developed CvP-LES turbulence closure:

1. is first-principles-based and removes unnecessary dissipation from any SGS model, allowing to tackle higher Reynolds numbers;

2. requires no spatial averaging of the dynamic parameter, since it is able to sense the local state of turbulence instantaneously adjusting of the SGS dissipation intensity;

3. is computationally inexpensive, easy to implement, requiring only one filtering operation on the enstrophy field (table 1);

4. discriminates regions dominated by coherent structures from fine-scale turbulence both *a posteriori* and *a priori*;

5. can be used to denoise and/or extract large-scale vortical motion from experimental datasets such as tomographic particle-image velocimetry (Tomo-PIV) of a turbulent flow;

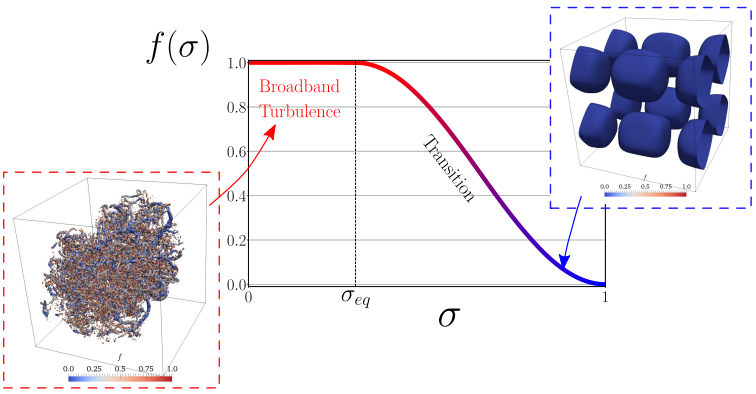

Figure 12: CvP eddy-viscosity correction function defined based on Eqn. (2). The cosinusoidal shape for $f(\sigma)$ guarantees a smooth transition of the eddy viscosity between large scale vortices and small-scale turbulence is chosen.

As shown in figure 12, the lower bound for $f(\cdot)$ is $f(\sigma = 1) = 0$, when the test-filtered enstrophy $\hat{\bar{\xi}}$ is equal to the primary-filtered enstrophy $\bar{\xi}$, hence no SGS dissipation should be applied. The upper bound, $f(\sigma_{eq}) = 1$, corresponds to fully developed equilibrium turbulence, based on which traditional SGS models are derived and hence should be applied. The value σ_{eq} is determined assuming the equilibrium energy spectral distribution predicted by Kolmogorov's theory [7, 28].

Application 1: Breakdown of Double Helical Vortex.

This task establishes the numerical framework and possible improvements for the study of transitional helical vortices and comparison with experiments. In this section, the application of the CvP-LES framework to a canonical setup of a pair of double-helical vortices is presented.

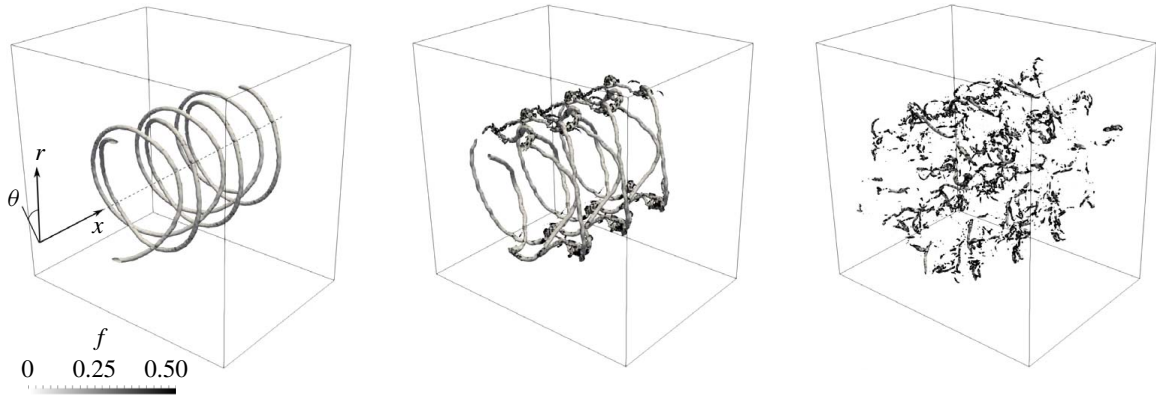

Figure 13: Iso-surfaces of vorticity coloured by the CvP–LES sensor function for three different times: before turbulent breakdown, during the vortex filament reconnection event and during the fully developed turbulent regime.

The numerical set-up for the study of the dynamics of helical vortices is first validated against the experiment of Nemes et al. [41]. One critical concern is the number of grid points defined to discretize the vortex cores when the flow is initialized. This directly impacts the prediction of the growth rate, α, which is based on the accurate identification of the vortex cores. Computations with 96^3, 144^3, 192^3 and 256^3 grid points resolve the initial vortex core of radius r_c with respectively 2.5, 4, 5 and 7 grid points. A grid convergence analysis based on the displacement rate and the energy spectra suggests that the 192^3 grid (i.e. 5 grid points across the initial vortex core) is adequate to represent accurately the range of relevant physical phenomena for the present validation study. Fig. 14(a) shows the growth rates of vortex-core displacement computed numerically as well as the exponential slopes determined in the experiments by Nemes et al. [41]. As seen from Fig. 14(a), a very good agreement is found between the simulations and experiment for the four different cases considered, thus corroborating the adequacy of the present numerical set-up for the study of transitional helical vortices subject to mutual inductance.

The dynamic evolution of a pair of double helical vortices is studied with CvP-LES for a range of parameter space (R and h being the helix radius and pitch, respectively.) Tested combinations of parameters include $h/R = 0.36$, 0.45 and 0.61, $r_c/h = 0.166$ and 0.333, Re_Γ=7000, 21000, and 70000. As a result, 18 computations for different combination of parameters are studied. For all the tested cases, the dynamic evolution of double helical vortex pair can be decomposed into three different regimes, represented on the enstrophy evolution in Figure 15, as a function of the non-dimensional time $t^* = t\Gamma/h^2$. From the beginning of the computation up to $t^* \approx 5$ (regime (A)), the flow dynamics is essentially inviscid, and the helical structures undergo relative displacements of their vortex cores with

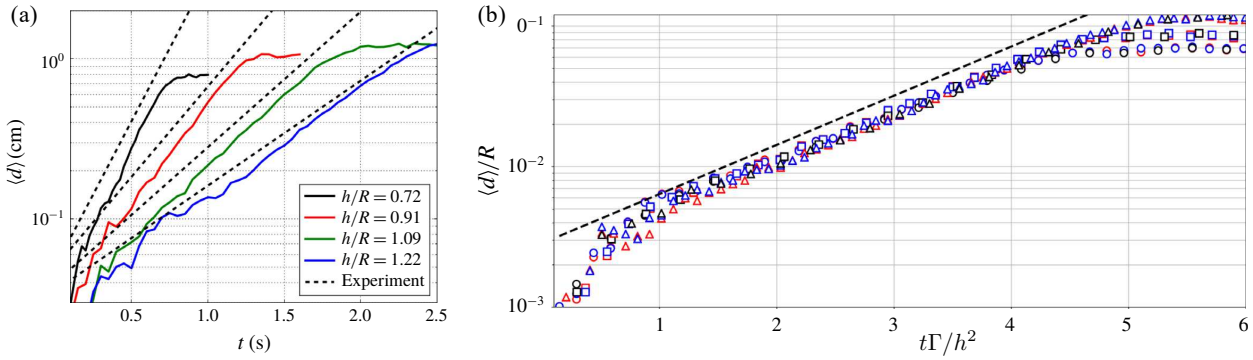

Figure 14: (a) Double helical vortex geometrical parameters with radius R and pitch h; (b) vortex-core displacement rates as a function of non-dimensional time $t\Gamma/h^2$ for vortex-core radius $r_c/h = 0.166$.

respect to the initial radius, induced by the mutual interaction between vortex filaments. During this first period, the volume-averaged enstrophy remains approximately constant in the flow as the vortices do not experience significant modification of their properties (vortex-core shapes and circulation). For this inviscid regime, growth rates of vortex-core displacements with respect to their rigid translation are studied over the parameter space and plotted as a function of non-dimensional time $t^* = t\Gamma/h^2$. As shown in Figure 14(b), in all the cases studied, the vortex-core displacement follows an exponential growth rate, i.e. $d(t) \propto \exp(at)$. The normalized $a^* = 2\pi a(2h^2)^2/\Gamma$ determined from CvP-LES simulations from all different cases collapse well together, yielding a value of $a^* \approx 20.2$. This value is very close to the value $a^* = 20.2$ measured in experiments [41], and those determined via linear stability analysis [17], which proves the validity of the CvP-LES simulation in capturing the dynamics of the coherent vortex structure accurately.

From $t^* = 5$ and onwards (regime (B)), we can notice a strong increase of enstrophy levels in the flow. The relative displacement of the vortex cores becomes significant enough such that the vortex lines become closer to each other and start interacting strongly, ultimately leading to the reconnection of vortex filaments at multiple locations on the helices. These vortex reconnection events generate small scales in the flow and modify significantly the shape of the initial helical vortices. The peak of enstrophy is reached when all the vortex reconnection events have occurred and all scales have developed in the flow. The time corresponding to the peak of enstrophy may vary depending on the flow parameters (Reynolds, helical pitch, initial vortex-core radius). After the peak of enstrophy is reached, the fully developed turbulent regime (C) is established.

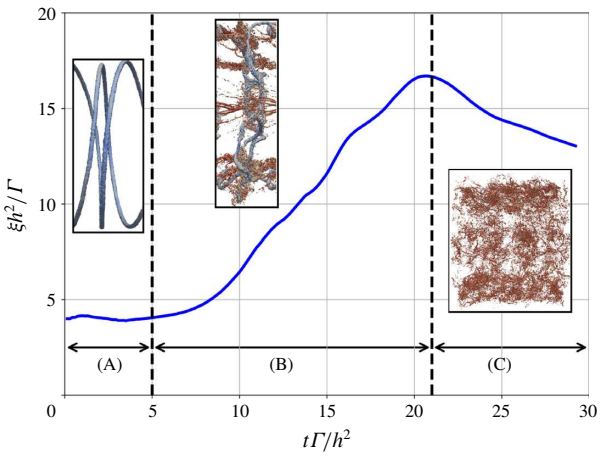

Figure 15: Flow regimes described from the evolution of volume-averaged enstrophy.

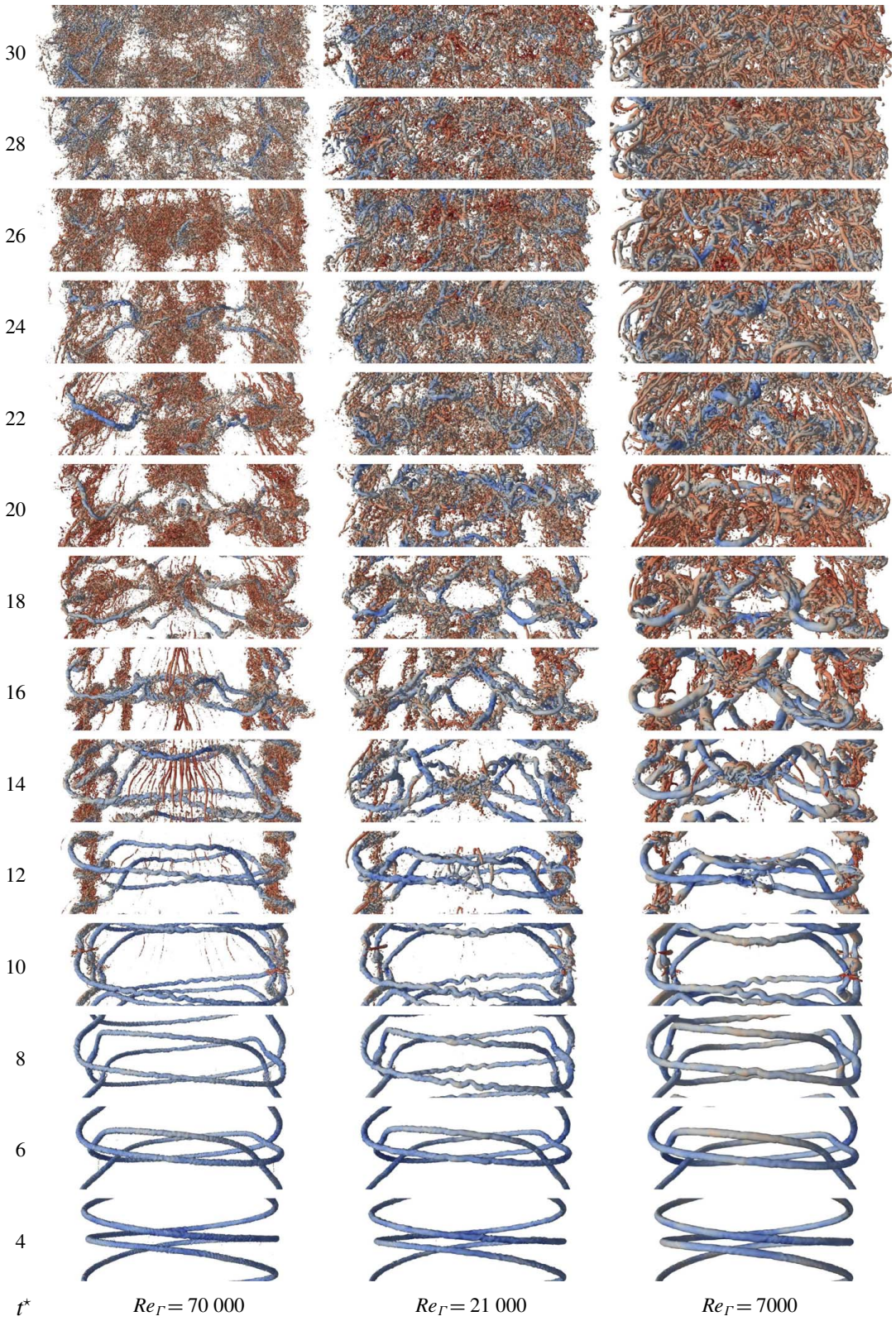

Figure 16: Q-isosurface colorred by pressure plotted at the beginning of transient regime starting from $t^* = 4$, for the helical pitch $h/R = 0.36$. The lowest core radius $r_c/h = 0.166$ case is considered.

The flow evolution is studied by inspecting the history of Q-criterion iso-surfaces at various times for all Reynolds numbers considered, comparing low and high helical pitches, as shown in Figures 16. At low-pitch configuration (Figure 16), short-wave sinusoidal oscillations are prominent on the vortex filaments as two helices are undergoing a leapfrogging motion. This has been experimentally observed by Felli et al. [14] in the context of the flow past marine propellers. The nature of these oscillations depends greatly on the Reynolds number. The highest Reynolds case displays small amplitude/small wavelengths oscillations, whereas at lower Reynolds numbers, the amplitude of the oscillations and their wavelengths increase. The two helices merge where the oscillation amplitude is the highest, form an X-shaped structure, pair and then reconnect with each other. The reconnection process is initiated by the formation of a series of secondary small scales, such as 'hook' structures that are perpendicular to the initial vortices, which shares strong similarities with the Crow instability [11].

A study of the turbulence anisotropy in the wake of the pair of helical vortices during the fully developed turbulence regime has been conducted. Calculations of the anisotropic Reynolds stress tensor have revealed a strong anisotropy for all cases, with a dominant axial component compared to the radial and azimuthal fluctuations, which are equal. The computation of the Lumlely invariants shows that increasing the helical pitch or Reynolds number reduces the turbulence anisotropy, whereas a larger initial vortex-core radius strengthens the anisotropy. A scale-by-scale anisotropy study showed that the axial integral scale is directly proportional to the helical pitch. The large scales are found to be anisotropic, with an elongation in the axial direction compared to the radial direction. This large-scale anisotropy is also propagated to smaller scales, as found by computing the moments of vorticity gradient ratios in various directions.

Application 2: Evolution of Coherent Trefoil Vorticies.

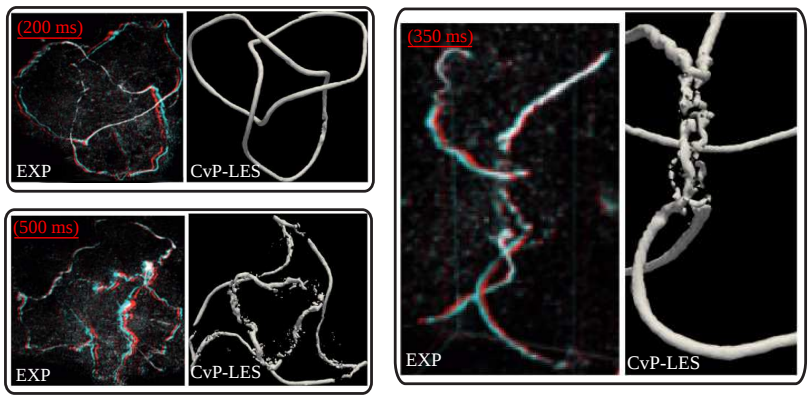

Figure 17: Comparison of flow topology between present CvP-LES and experiments by Kleckner and Irvine [27] before, during and after the vortex entanglement process.

The goal of this Task is to establish and validate a numerical setup for the study of entangled knotted vortices dynamics targeting the experimental results of Kleckner and Irvine [27]. The study of entangled vortex filaments is of interest since most of turbulent flows show the presence of such phenomena, as demonstrated by Direct Numerical Simulations of other turbulent flows [23, 25, 52, 57]. We show in this study with CvP-LES that good qualitative matching has been achieved against the experiments by Kleckner and Irvine [27] (figure 17) for the three different times considered: before, during and after the vortex bursting process. The

CvP-LES simulation results, in resolved coherent vortex kinematics and modeled turbulent statistics with CvP-LES method, are validated with fully resolved AMR-DNS later on at low and moderate Reynolds numbers $Re_\Gamma = 2000$ and 6000.

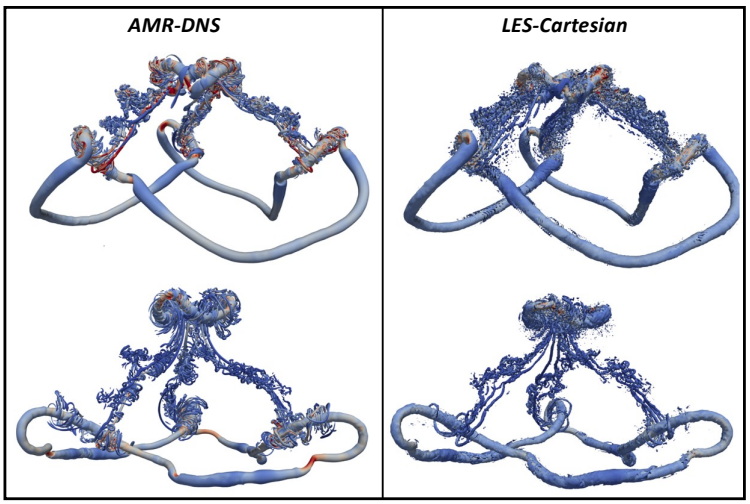

Figure 18: Comparison between the Q-isosurfaces between AMR-DNS and LES at two different time steps during reconnection.

In the experiment conducted by Kleckner and Irvine [27], a trefoil knot vortex-shaped hydrofoil had to be manufactured using a 3D printer and used to generate a knotted via a quick displacement of the hydrofoil in a water tank (Figure 17). In our numerical setup, a knotted vortex path is defined using a parametric equation, and the corresponding initial velocity field is assigned via Bio-Savart law, coupled to a smoothing kernel function allowing to control the vortex core radius. The initial knotted vortex propagates along, and rotates about the same axis (as seen from Figure 25 in the next section), then gradual distortion and elongation of the vortex filament are observed, due to the self-induced convection velocity of the smaller radius portion of the knot ($R(\theta) < \bar{R}$) being higher than that of the outer portion ($R(\theta) > \bar{R}$). This leads to the stretching of the vortex line ($t^* \approx 1.97$) and three simultaneous reconnections of vortex filaments ($t^* \approx 2.59$). After this reconnection event, two distinct vortical structures initially triangular in shape are generated, which then evolve following independent dynamics ($t^* \approx 3.94$).

The advantage of using CvP-LES method to study this problem is to accurately predict the kinematic propagation, topology transition, and the whole reconnection process of the large-scale coherent vortex structure without overkilling the large scales with artificial dissipation, or without resolving the large amount of small scales generated during the reconnection process using unaffordable computational resources. As shown in figure 19, the CvP sensor function $f(\sigma)$ is capable of detecting the under-resolved small-scales generated during the reconnection process, and applying SGS dissipation only to those regions. As shown in Figure 20(left) the total dissipation (resolved plus modeled via CvP) recovers the peak dissipation calculated from the DNS. Before and after reconnection, the CvP-sensor prevents the SGS from spuriously dissipating the coherent vortex struc-

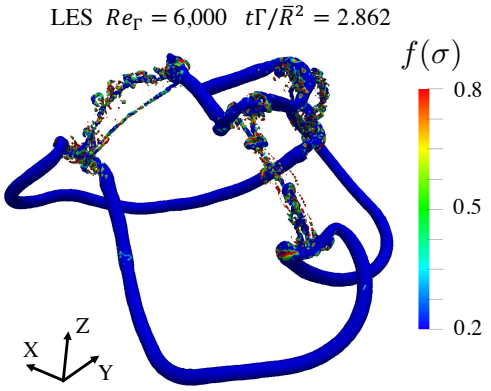

Figure 19: Sensor function $f(\sigma)$ used in the CvP-LES closure in Eq. 2 at a specific time from an LES simulation at $Re_\Gamma = 6,000$.

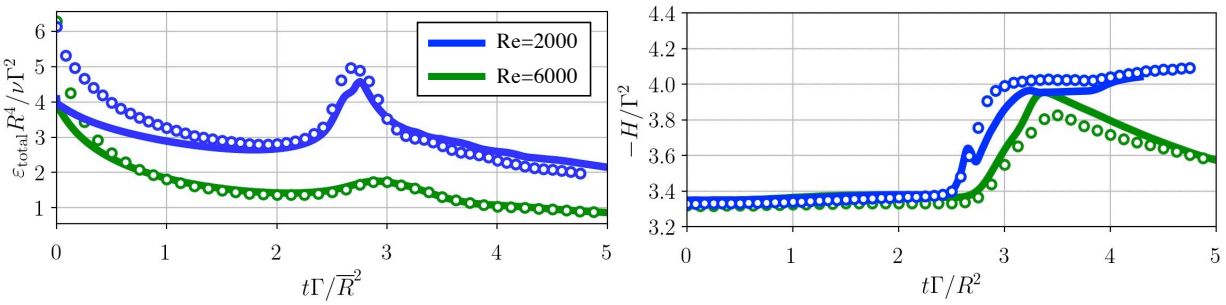

Figure 20: Dissipation (left) and total helicity (right) for the trefoil knotted vortex at two different Reynolds numbers: Re_Γ=2000 (green) and 6000 (blue). The solid lines stand for the fully-resolved DNS, and circles for CvP-LES.

ture, by preventing the SGS stress from being applied to the large-scale vortex parts. In this way, the large-scale kinematics of the vortex evolution are well preserved, as seen from the right column of figure 18. Also, the SGS stresses contribute significantly to the dissipation of the helicity occurring during reconnection, allowing to recover the peak value of helicity decay rate $-dH(t)/dt$ predicted by the DNS calculations. This directly contributes to the successful prediction of the evolution of the total helicity as shown in Figure 20 (right) at two different Reynolds numbers.

Figure 18 shows a side-by-side comparison between DNS and LES simulations each stage of vortical flow evolution mentioned above. In comparison, LES results preserve the evolution of large scale structure without resolving the fine-scale turbulent structure generated via reconnection. As shown in Figure 19, the CvP sensor function $f(\sigma)$ is capable of detecting the under-resolved small scales generated during the reconnection process, and applying SGS dissipation only to those regions. The result showcases the capability of accurately predicting the behavior of large-scale vortex structures over long period of time and through complicated vortex interactions.

Accomplishment 2: DNS via Adaptive Mesh Refinement

Methodology

The adaptive mesh refinement framework of VAMPIRE code is developed and modified based on Paramesh [35]. The computational domain is discretized by a number of blocks, and each block has the same number of uniformly spaced grid points inside. A error detection function is evaluated for all blocks, based on the respective error detection value, the block is determined whether to be refined or coarsened. A tree data structure is utilized, where a coarse block is refinement into a number of finer blocks, the finer blocks are linked to the original coarse block as its child blocks. The child blocks are overlapping the same domain as their parent block does, but with grid spacing finer by a factor of refinement ratio γ. In this study, the refinement ratio is fixed to be 2, which means after one time of refinement, a parent block is divided in each direction into two blocks. In a 3D simulation, one parent block has 8 child blocks, while in a 2D simulation, one parent has 4 child blocks. The tree data structure facilitate the efficient searching for neighbors and optimal sorting for load balancing.

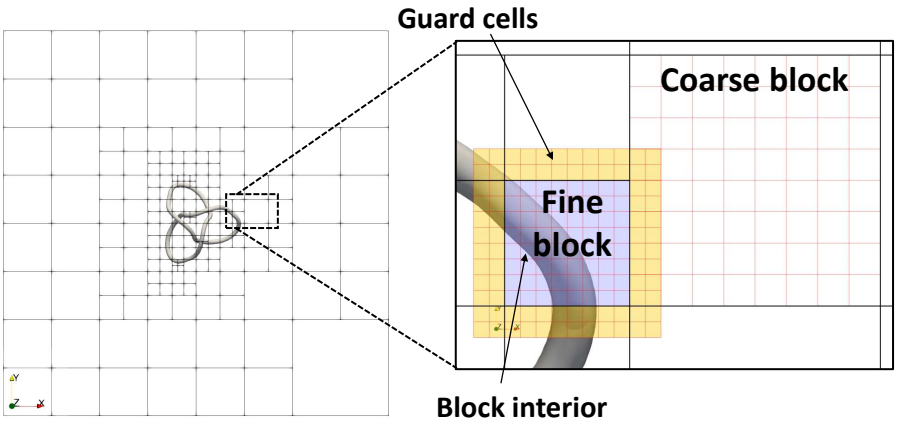

Figure 21: The guardcells in a multi-level grid: according to their location, three highlighted regions represent cell-boundary interface, coarse-fine interface, and interface between same level neighbor blocks.

The AMR code VAMPIRE is aimed on heavy MPI computation, and load balancing is performed at the end of each time step. According to the newly resulting tree structure (as shown in Figure 22), a space-filling curve (also called Morton curve) is drew passing through all the leaf blocks, and associated numbering for each block is generated Then with the numbering, the blocks are allocated to all the available processors. This method ensures the maximization of locality of neighbor blocks and parental blocks, and therefore the minimization of MPI communications.

The solution on each block depends on its surrounding, and this is achieved by filling the guardcells of each block. Guardcells are the additional layers of cells surrounding the current block. The guardcell values are filled based in the information from the surrounding blocks via MPI operation. In the case that the portion of guardcell is on the interface between

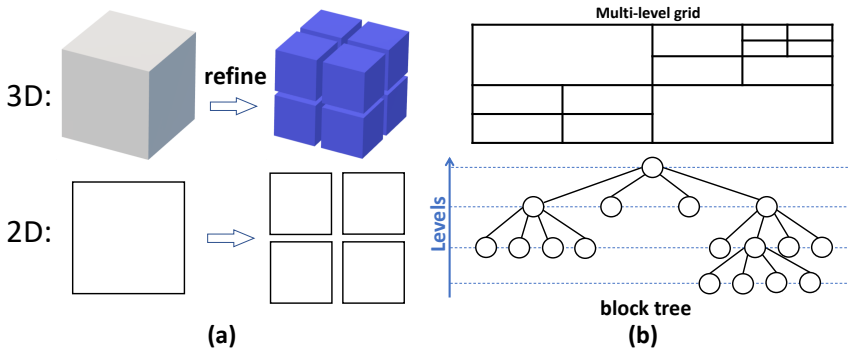

Figure 22: The guardcells in a multi-level grid: according to their location, three highlighted regions represent cell-boundary interface, coarse-fine interface, and interface between same level neighbor blocks.

coarse and fine blocks, prolongation and restriction operation is needed for filling this portion of guardcell values. Higher-order interpolation function can be used to achieve higher order accuracy in such coarse-fine guardcell-filling situation, and this typically requires more layers of guardcells. Besides, guardcells are also used to impose boundary conditions, in case that a block is located adjacent to physical boundaries.

The compact operators are global operators that all the points in the computational domain are involved and a matrix inversion is needed for solving the interpolated/differentiated values. Whereas in the multi-block AMR approach, each compact operator is restricted within its block, and guardcells are used for the inter-block communications. Therefore, these compact operators are discontinuous at the block interfaces. This will not influence the order of accuracy, in the case that the neighbor blocks are on the same level of refinement, in which the guardcell filling operation is done with point-to-point copying the value from neighbor blocks to its guardcells. With designed numerical scheme, all the leaf blocks can achieve an overall 4th order of accuracy. However, in the case of multi-level grid, the overall accuracy is throttled by the order of accuracy of the prolongation/restriction function, where additional interpolations are employed. In this work, 2 layers of guardcells allow up to 4th-order for the polynomial interpolation for prolongation/restriction function. With 4th-order polynomial interpolation, the overall order of accuracy is tested on a multi-level grid to be also 4th-order, which is acceptable for current purpose.

Application: Vortex Reconnection at High Reynolds Numbers

The adaptive mesh refinement (AMR) high-order compact finite difference code VAMPIRE is used to perform a DNS simulations of the knotted vortex reconnection for two different Reynolds numbers. The two Reynolds numbers under study are selected to be a moderate Reynolds number Re_Γ=2000, and a high Reynolds number Re_Γ=6000. For each simulation, before time advancement, a sensor estimating the discretization error of the sampled initial condition is ran on all the blocks to determine whether the mesh should be locally refined; such process is repeated until convergence of the AMR tree structure. Fig. 6 is a showcase of resulting adaptively refined mesh starting from $t^* = 0$ and subsequent times for Re_Γ=6,000.

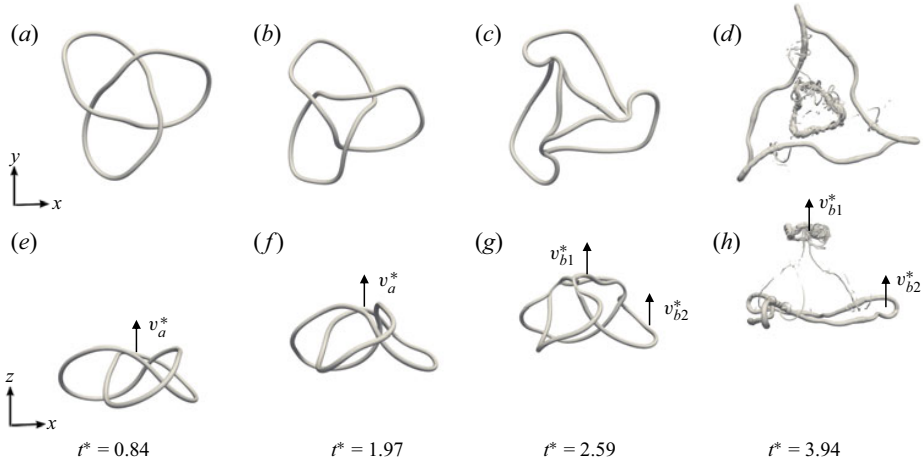

Figure 23: Visualizations of Q-isosurfaces with $QR^4/\Gamma^2 = 97$ extracted from $Re_\Gamma = 6000$ simulation. Here v_a^* denotes the dimensionless propagation velocity of the knot before reconnection ($t^* < 2.5$); v_{b2}^* and v_{b1}^* denote the small and large rings velocity, respectively, after reconnection.

The first subject of investigation is the kinematic evolution of the vortex structure, and the influence of Reynolds number on it. The vortex kinematics before and after the reconnection are similar among the different Reynolds number investigated, the flow dynamics during the reconnection are strongly affected by viscous forces. The latter are responsible for intense enstrophy and helicity production events, which intensify with Re_Γ.

The propagation velocity of the initial knotted structure, v_a, and of the smaller, v_{b1}, and larger, v_{b2}, vortex rings forming after reconnection (Figure 25) can be evaluated via curve-fitting in the z-t plane based on the local maxima of vorticity magnitude in the x-y plane. The corresponding non-dimensional expression can be obtained based on the initial circulation Γ_0 and the mean knot radius, $\overline{R}$: $v_a^*, v_{b1}^*, v_{b2}^*$. The values of v_a^* extracted from present calculations are similar between two Reynolds number, justifying the use of the inviscid scaling $t^* = t\Gamma/\overline{R}^2$ before the first reconnection. This can be explained that the core size difference caused by the Reynolds number is negligible compared to the length scale of the coherent vortex structure before reconnection, therefore thin-core assumption still holds well and its influence is very little on the overall kinematics.

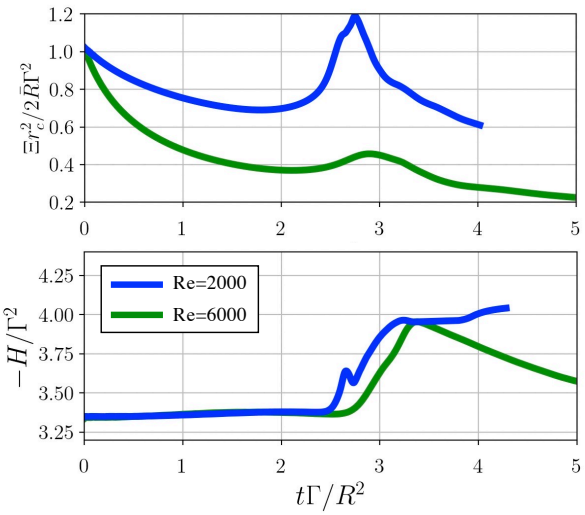

Figure 24: DNS-AMR simulation data for the evolution of enstrophy and total helicity for the trefoil knot at Re_Γ=2,000 and 6,000 .

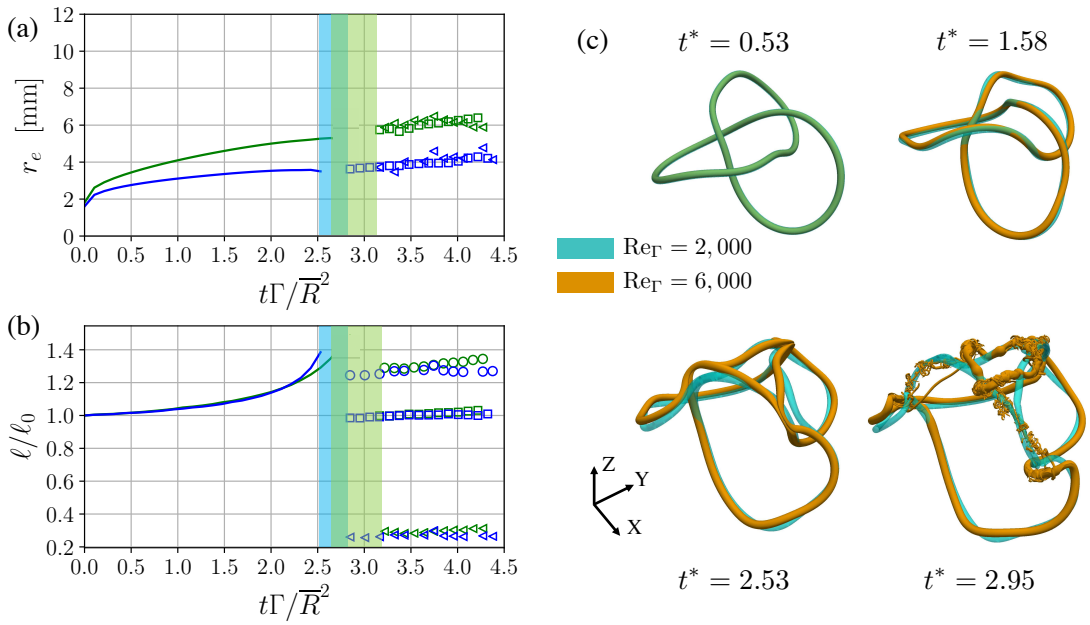

Figure 25: (a) Evolution of effective core radius r_e and (b) instantaneous vortex length $\ell(t)$ normalized by the initial vortex length ℓ_0 for Re_Γ=2,000 (green) and 6,000 (blue). Regions shaded via vertical bars represent the time intervals when reconnection is happening. Solid lines are used before reconnection; □, △ and ○, for small, large ring and their sum after reconnection respectively.

In this study, the vortex centerline (shown in Figure 25) is extracted based on eigenmodes of the velocity gradient tensor following an approach, and the boundary of the vortex tube is identified by applying a regression fit of the vorticity distribution to a Lamb-Oseen model on a cut-plane perpendicular to the vortex line. The effective core radius r_e in this work is taken as twice r_c in order to effectively cover around 95% of the vorticity in a vortex tube of diameter $2r_e$. As shown in figure 25 (a), before the reconnection happens, the core radius for the Re_Γ=2,000 case is about 1.7 times compared to the Re_Γ=6,000 case, which satisfies the scaling law $r_e \sim \sqrt{\nu t}$. The finite core size effect on the induced velocity shows up at about $t^* = 2.2$ where the two vortex length curves peel off from each other, signifying that two vortex segments are getting close to each other more rapidly for the higher Reynolds number case. The vortex stretching occurs much faster in the Re_Γ=6,000 case, resulting in earlier reconnection. The reconnection process lasts longer at lower Reynolds number, which can also be linked to the thicker core size at Re_Γ=2,000. The analysis on the core radius and the centerline kinematics suggests that Reynolds number influences the knotted vortex dynamics in two different ways: one is via affecting the core radius, and another way is via the generation of small-scales during the vortex interaction.

Figure 24 shows the global statistics for volume-integrated enstrophy and helicity. The abrupt production of enstrophy and helicity signifies the reconnection event for each Reynolds number condition. Aligned with the observations from the vortex centerline kinematics (Figure 25), reconnection happens earlier at the high-Re case. The enstrophy generation is way stronger in the Re_Γ=6000 case compared to Re_Γ=2000, standing for the strong generation of

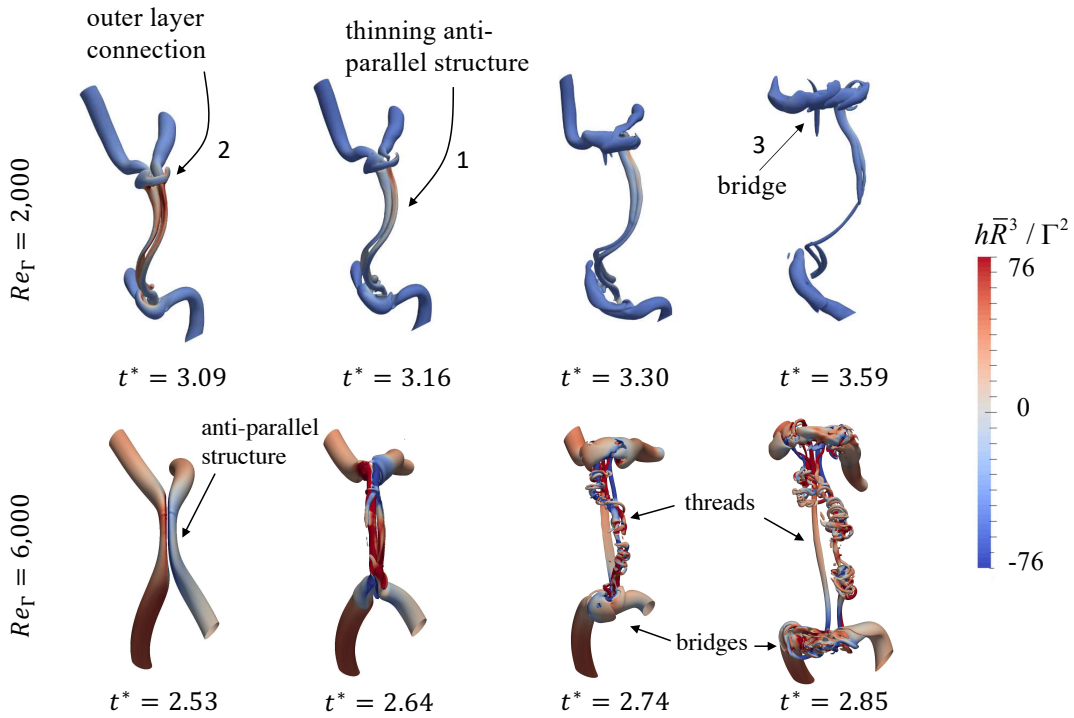

Figure 26: Visualization of the generation of hairpin vortices from Q-isosurfaces at $Q\overline{R}^4/\Gamma^2 = 96$ *for* $\mathrm{Re}_\Gamma = 2{,}000$ *and* $\mathrm{Re}_\Gamma = 6{,}000$ *from DNS/AMR data, colored by normalized helicity density; threads created during the* bridging *process, intermediate hairpin vortex structure the final dominant hairpin structure are illustrated.*

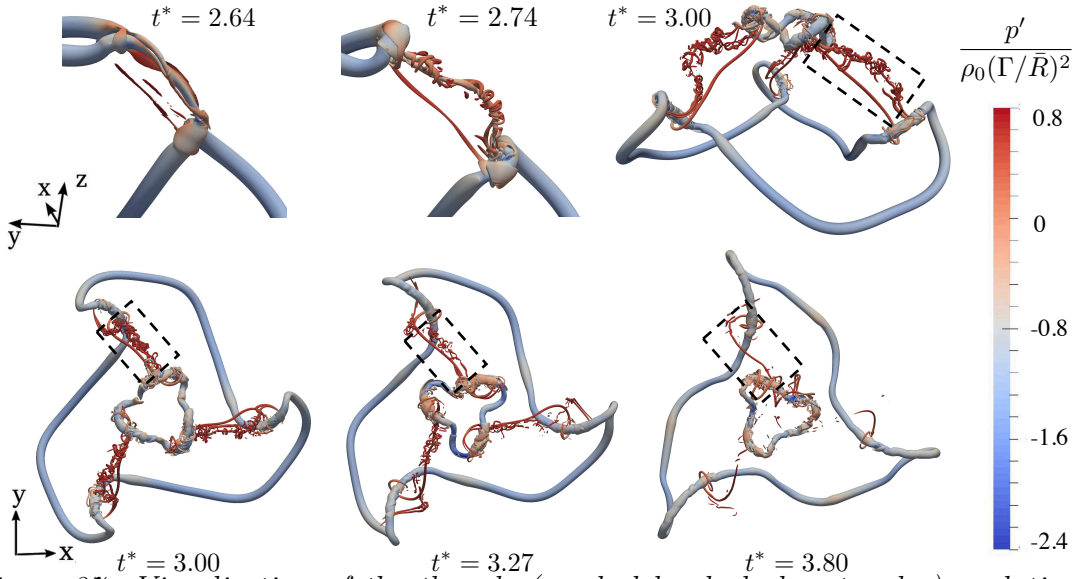

Figure 27: Visualization of the threads (marked by dashed rectangles) evolution using Q-isosurfaces with $Q\overline{R}^4/\Gamma^2 = 323$ *for* $\mathrm{Re}_\Gamma = 6{,}000$ *DNS colored by normalized pressure fluctuations (Structure* $\langle III \rangle$*).*

small-scale vorticity structures through the reconnection event, and resulting in much higher viscous dissipation of kinetic energy.

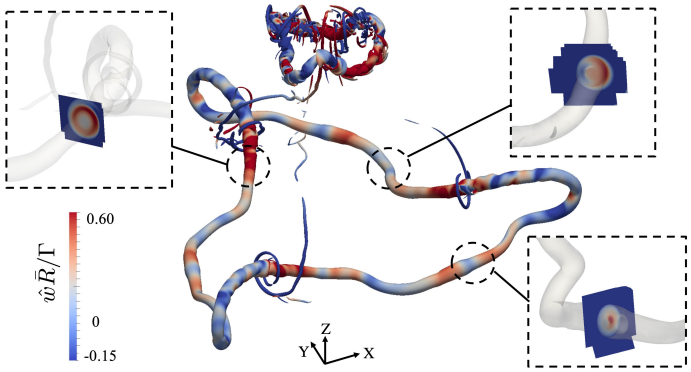

Figure 28: Axial flow distribution ($\hat{w}$) on three different cutplanes on the large vortex ring after reconnection based on the Q-isosurface and Re_Γ=6,000 from DNS results.

The study of the vortex structure and the comparison between two Reynolds number condition is another focus of this DNS study. Figure 27 shows the comparison of the vortex structure at two Re cases via the visualization of Q-criterion. During the evolution of a knotted vortex, the generation of four characteristic vortical structures can be identified: $\langle I \rangle$ anti-parallel structures; $\langle II \rangle$ hairpin vortices; $\langle III \rangle$ thread structures; $\langle IV \rangle$ helical modes (also named Kelvin waves). Events leading to the formation of such structures are observed for both Reynolds numbers considered. Structures $\langle I \rangle$ and $\langle II \rangle$ form simultaneously and participate in the bridging process. The thread structures $\langle III \rangle$ connect the large and small vortex rings during the last stages of reconnection, which culminates with the complete separation of the two rings and the corresponding initialization of helical, or Kelvin waves $\langle IV \rangle$. The latter, via nonlinear collisions, lead to repeated (in time and space) momentary ruptures (or burstings) of the vortex topological structure. Some detailed, fully resolved vortex structures at Re_Γ=6000 are shown in Figure 27.

Helicity is related to the topological features of the flow, like the degree of knottedness, and linkage, as discussed by [51]. Knotted vortices are of interest for the study of helicity dynamics due to their non-zero initial global (or total) helicity, H, which is determined by the initial filament topology; for a single vortex ring the initial global helicity is, in fact, zero. We assess here the sensitivity of the total helicity evolution to the Reynolds number with thin initial vortex core radius $r_e/\overline{R} \approx 0.06$. We also report our analysis on three quantities derived from the helicity density $h = \mathbf{u} \cdot \boldsymbol{\omega}$: total helicity, $H(t)$; centerline helicity, $H_C(t)$; and vortex-tube integrated helicity $H_V(t)$.

Total helicity $H(t)$ is integrated across the entire computational domain,

$$H(t) = \iiint_{-\infty}^{+\infty} \mathbf{u} \cdot \boldsymbol{\omega} \, \mathrm{d}\Omega \approx \int_0^L \int_0^L \int_0^L \mathbf{u} \cdot \boldsymbol{\omega} \, \mathrm{d}\Omega \tag{3}$$

and it contains information from all the scales in the flow. Centerline helicity $H_C(t)$ is defined as

$$H_C(t) = \Gamma \oint \tilde{w}|_{\tilde{r}=0} \, \mathrm{d}\ell, \tag{4}$$

which is useful in theoretical analyses assuming infinitesimally thin vortex tubes with confined helicity. This practically accessible form is adopted by [51], where $\mathrm{d}\ell$ is the infinitesimal length of a line element along the loop, and $\tilde{w}$ as a function of $\tilde{r}$ is the local axial velocity. Centerline helicity, $H_C(t)$, is also reported by [51] to be approximately conserved during reconnection in a viscous flow, which is also confirmed by the results in the present study.

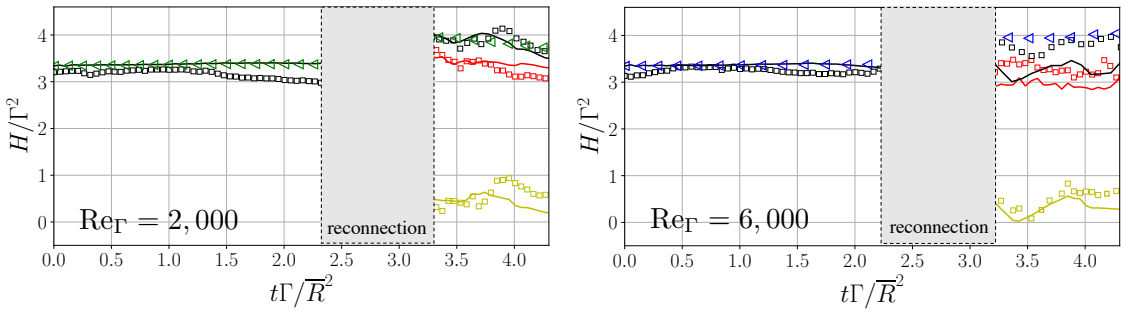

Figure 29: Evolution of centerline helicity $H_C(t)$ (—), tube-integrated helicity $H_V(t)$ (□), and total helicity, for the entire vortex structure (black), and small leading ring (yellow) and large trailing ring (red) after reconnection. Green and blue triangles (◁) show the normalized total helicity $H(t)$ for $Re_\Gamma = 2{,}000$ and $Re_\Gamma = 6{,}000$, respectively. The gray box is masking the reconnection time when the vortex centerline is not clearly defined.

Finally, the vortex-tube-integrated helicity is defined as

$$H_V(t) = \iiint_V \mathbf{u}\cdot\boldsymbol{\omega}\ \mathrm{d}\Omega \tag{5}$$

where the volume of the vortex ring V is defined as the region with distance smaller or equal to r_e from the vortex core. In the limit of $r_e \to 0$, Eq.(5) yields Eq.(4). The vortex-tube-integrated helicity can be seen as an improvement upon Eq.(4), as it allows to take into account the inner structure of a finite-thickness vortex core.

Figure 24 (bottom) shows the total helicity evolution $Re_\Gamma = 2{,}000$ and $Re_\Gamma = 6{,}000$. Both of them show a similar but clear stages of temporal development: in the first stage, the total amount of helicity almost stay constant, because in this stage, the vortex evolves in an inviscid manner, and the knot structure preserves the helicity values. The second stage starts as the helicity start to rapidly increase. This second stage in helicity evolution corresponds to the reconnection event where the vortex knot decouples to two separated rings. The trend in the second stage is similar regardless of Reynolds number, whereas the onset time of the second stage is slightly earlier for the high Reynolds number condition, due to the earlier starting time for the reconnection at Re_Γ=6000. The only obvious difference in the growing stage is that the Re_Γ=2000 case gives a nearly linear growth, whereas the Re_Γ=6000 case shows some non-linearity and fluctuations in the growth. The third stage starts as the total helicity curve reaches its peak and finishes its rapid growth, and after the peak, the the total helicity curve shows a steady decay for the Re_Γ=2000 case and some random fluctuation for the Re_Γ=6000 case. The model raised in Accomplishment 3 provides the explanation for these regimes, which will be discussed in details in the next section.

In addition, the validity and accuracy of the two simplified representation of the helicity content: centerline helicity H_C Eq.(4) and tube-integrated helicity H_V Eq.(5) will be checked against the fully resolved total helicity H, which serves as a reference. As shown in Figure 29, before the reconnection event, both H_C and H_V gives very good matching to H, indicating that both of them can be used as a good estimate in experiments, etc. However, after the reconnection, the flow field becomes more irregular, the accuracy of H_C and H_V starts to be influenced. Also this accuracy is further reduced with Reynolds number being high, as shown in Figure 29 (right).

Accomplishment 3: Theory for Helicity Dynamics

Background

Total helicity, H, is a measure of the topological complexity of a tangled vortical flow field. It is defined as the integral of helicity density, $h = \mathbf{u} \cdot \boldsymbol{\omega}$, over the fluid domain surrounding the vortex field. Total helicity is a conserved quantity in inviscid flows, as found in superfluids [24, 44], however, it may increase or decrease in the presence of viscous effects. The latter are always dissipative in nature and are responsible for the annihilation of negative/positive helicity density, resulting a total helicity increase/decrease. The rate of change of total helicity, dH/dt, is proportional to the super-helicity, $\langle s \rangle \equiv \langle \boldsymbol{\omega} \cdot (\nabla \times \boldsymbol{\omega}) \rangle$ through the kinematic viscosity ν . The understanding of helicity dynamics is of crucial importance in a wide variety of fields, such as liquid crystals [56], optical [12], biological structures [10, 20], and beyond.

In the case of viscous vortex flows, tangled vortex fields tend to evolve towards simpler topologies. Knot and link are two basic states of tangled vortex fields, which are explored in this manuscript; unknotting and unlinking are the respective processes responsible for their break down into a simpler topology, and hence change in total helicity. Recent experimental studies [27,51] have revealed how the zeroing of total helicity during the unknotting of vortex rings does not happen abruptly. In fact, during the unknotting process the measured helicity appeared to be 'relatively' unchanged. However, due to the presence of a broad spectrum of small spatial and temporal scales unaccessible by the experiments, a clear demonstration as to whether helicity is conserved or not through such reconnection events has been deemed unclear by [40]. Accurate direct-numerical simulations able to simultaneously capture the entirety of the topologically complex vortex field and the small-scale details of the viscous reconnection are thus warranted. This is only achievable by relying on Adaptive-Mesh Refinement (AMR) code VAMPIRE (Accomplishment 2).

This part of the work under the support of YIP is focused on deepen the understanding of the vortex dynamics and helicity dynamics of vortex fields undergoing unknotting and unlinking processes initiated by local viscous reconnection events. The goal is to obtain a theoretical model that explains the drastic helicity dynamics observed in the DNS/LES simulations for entangled vortex field with topological complexity.

A Four-Element Mechanistic Model

In viscous fluids, topology is manifested in the form of vortex structure. Vortex structure with topological complexity has two basic forms: knots and links. Because of the presence of viscosity, the vortex topology will tend to evolve in viscous fluids into topologically simpler structure. In this transition, there will be a topology-change event, through which the topology changes from knots or links to one or a series of trivial typologies, such as rings. In viscous fluids, such an event is realized via vortex reconnections. In terms of helicity statistics, total helicity is not conserved through reconnection in topologically complex vortex problems, and that this occurs through a process of annihilation of the local helicity content caused by circulation transfer. Before reconnection event, the vortex topology structure will evolve itself in an inviscid manner to a locally anti-parallel structure, as the onset

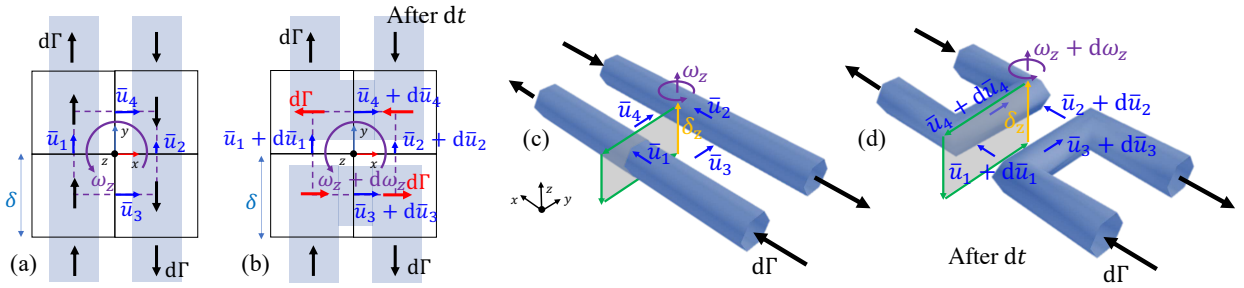

Figure 30: (a,b) Kinematics of a reconnection of infinitesimal vortex filaments with a discretization by cells with edge length of δ; (c,d) the reconnection site viewed from a different angle, with the Stokes surface highlighted.

posture signifying that a reconnection event is ready to get started. Figure 31 shows a typical pre-reconnection configuration commonly seen in a reconnection event. The large scale super-helicity structure, as shown in Figure 31, exhibits a two-pair petal shape, where the red and blue petals represent the positive and negative super-helicity clots, respectively. Such a structure is determined by the curvature of centerlines, and the sharp gradient of vorticity magnitude formed by the anti-parallel vorticity field. However, the local helicity content, which is not represented by the petal structure and is dictated by the fluid velocity parallel to the local vortex line, plays a dominant role in the net helicity change through this reconnection event, and can be understood via a linearity four-element circuit model.

Figure 30 shows the 4-element model to explain the mechanism of the helicity annihilation over the reconnection event, with the assumption that the circulation transfer happens in a 2D plane, on which the four elements stand. Each element represents a finite volume, with a length scale δ in each direction. Their cell-averaged velocity and circulation (vorticity) are represented with u_i and ω_i, where i is the cell index, with the values from 1 to 4. During a reconnection event, the circulation is transferred over time from y-direction to x-direction. For analytical analysis, we can consider that over an infinitesimal time period dt, there is a dΓ amount of circulation decrease in y-direction, and a same amount of dΓ amount of circulation increase in x-direction. The calculus in deriving the final expression (the details can be seen in the Appendix C of [63]) shows that the contribution to the helicity given by the change of velocity field and vorticity field under external influence from the flow field can be considered independently. As only the vorticity change is related in the discussion of circulation transfer, and velocity change is an independent event that happens regardless the existence of circulation transfer, here it can be assumed that velocity components (i.e. u_i) are unchanged

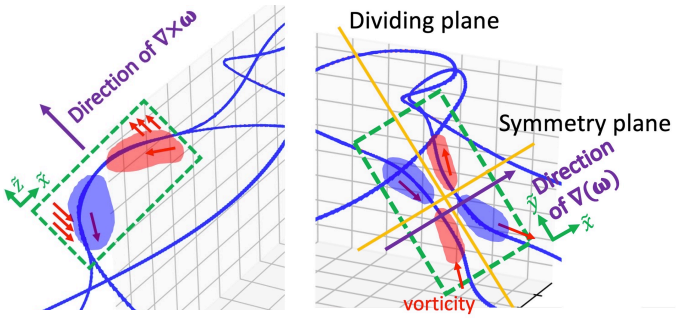

Figure 31: Qualitative plot of selected vortex lines during the interaction of anti-parallel vortex tubes (red, threads; blue, reconnected bridges). The arrows form a loop enclosing a plane through which one of the vortex tube passes.

over the time dt.

As the null axis in the center of the reconnection zone (yellow arrow in Figure 30), the vorticity component perpendicular to the reconnecting plane ω_z can be expressed with the surrounding velocity components:

$$\omega_z = (-\bar{u}_1 + \bar{u}_2 + \bar{u}_3 - \bar{u}_4)/\delta. \tag{6}$$

This vorticity component is not participating in the circulation transfer, because the reconnection is 2D and only happens in the x-y plane, as assumed by the four-element model. However, the ω_z component is dictated by the local helicity content, and directly contributes to the helicity change rate. Applying Stokes theory to the plane enclosed by the green-yellow arrows in Figure 30 (c,d), the following expression can be obtained:

$$\dot{\Gamma} \equiv \frac{\mathrm{d}\Gamma}{\mathrm{d}t} = -\nu \oint_{\delta A} (\nabla \times \boldsymbol{\omega}) \cdot \mathrm{d}\mathbf{l}, \tag{7}$$

Together with the helicity change within each small element over dt, a final expression can be obtained:

$$\frac{\mathrm{d}H}{\mathrm{d}t} = -\frac{\mathrm{d}\Gamma}{\mathrm{d}t}\frac{\mathrm{d}H_1 + \mathrm{d}H_2}{\mathrm{d}\Gamma} = -2\delta(\bar{u}_1 - \bar{u}_2)\dot{\Gamma} \tag{8}$$

where $\mathrm{d}H_1 = 2\delta\bar{u}_1\mathrm{d}\Gamma$ and $\mathrm{d}H_2 = -2\delta\bar{u}_2\mathrm{d}\Gamma$ are the helicity content stored in the reconnected segments of the two vortex tubes. This expression indicates that the local helicity change rate at the reconnection spot can be written as the product of the local circulation transfer rate and the local helicity content carried by the reconnected segments of the vortex tube.

Applications: Knotted Vortices, Linked Vortices, and Colliding Vortices.

The model can be used to provide insight into results from simulating vortex dynamics with topological complexity with DNS and LES. In this section, the mechanistic model described above is applied several different vortex topologies. Three sets of topologies are simulated with VAMPIRE code at Re_Γ=2000, with four different initial vortex core thicknesses. Three configurations, namely, trefoil knot, two-ring link, and a pair of colliding rings, are shown in Figure 32. These three configurations are selected to include the simplest forms of knot and link, as well as the simplest topologically trivial configuration with reconnections (i.e. colliding rings). In all the configurations, the initial flows are initialized with analytical equations in parametric form. After initialization, all of them evolve to one or multiple locally anti-parallel vortex structures, before reconnections happen. As all the configurations are designed to be symmetric, for the cases with multiple reconnection sites, all the reconnection processes happen and end at the same time.

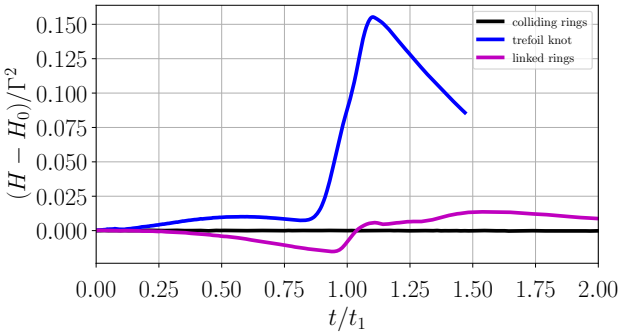

Figure 33: Total helicity is compared to trefoil knot and linked rings, plotted versus time normalized by the reconnection time t_1.

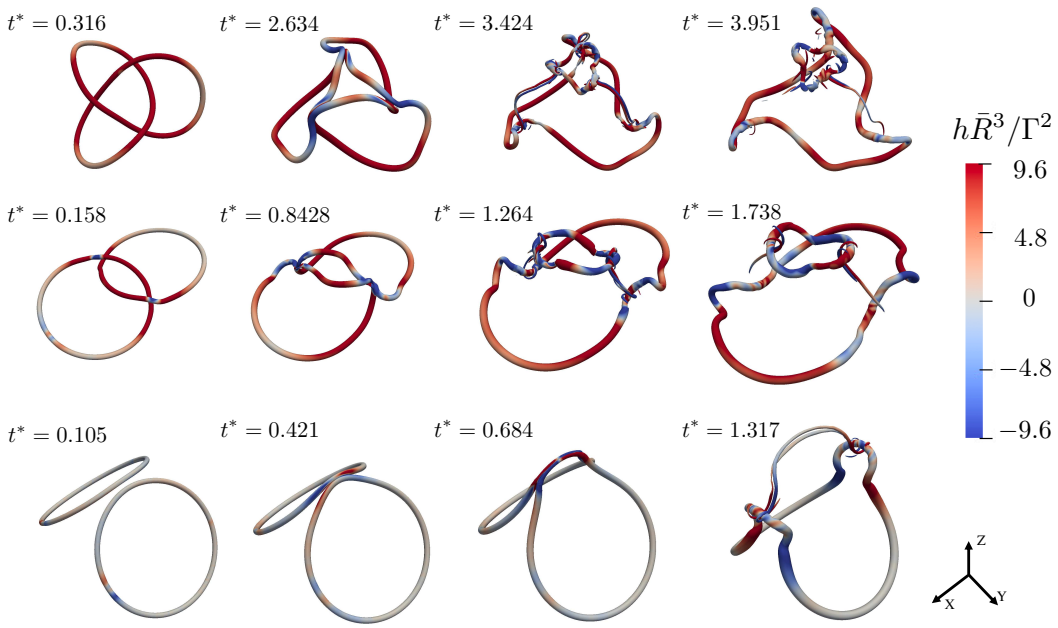

Figure 32: Isosurfaces of $Q\overline{R}^4/\Gamma^2 = 323$ at different times colored by helicity density for trefoil knot (top), two-ring link (middle) and colliding rings (bottom) for r_c=2 mm.

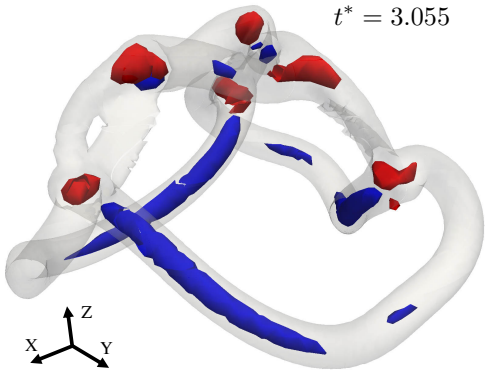

Figure 34: Isosurfaces of super-helicity $-s\bar{R}^5/\Gamma^2 = \pm 2730$ (red and blue) at $t^* = 3.055$.

Figure 35 shows the global helicity statistics for the knot cases and the link cases. All of them shows a period of drastic change in helicity, which designate the process of reconnections. It also shows that the vortex core thickness affects the the helicity dynamics significantly. With thinner vortex core, the reconnection happens and finishes in a faster fashion, corresponding to a steeper slope in the global helicity statistics. In contrast, thicker vortex core (indicating weaker vortex strength) results in flatter change in helicity.

Comparison between the knot and link with the reconnection with trivial topology (i.e. colliding rings) change shows significant difference, as shown in Figure 33. It is clear that the drastic helicity change only happens in reconnections of non-trivial vortex topologies, and no change (as shown by the black line in Figure 33) for reconnections without topology changing. This suggests that the helicity 'jump' is not a necessary product of vortex line reconnections, but is a direct result of topology change.

Furthermore, the super-helicity structure in petal form in a realistic vortex reconnection event discussed in the previous section are depicted in Figure 36 (a). When vortex line reconnection is happening, the anti-parallel vortex tubes are highly compressed, resulting in extremely thin and symmetrical petal structures. Figure 36 (b) shows the helicity density structure in the trefoil knot with r_c=2 mm. Unlike super-helicity structure, the helicity

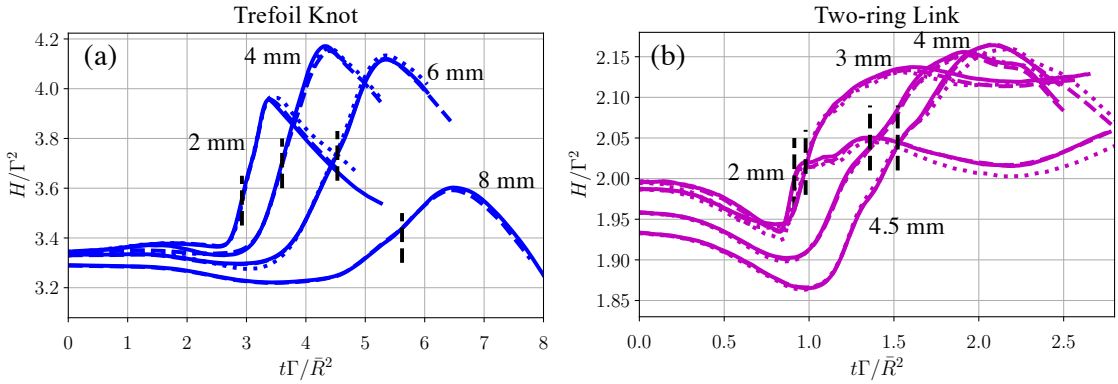

Figure 35: Total helicity H for trefoil knot (subplots a in blue) and two-ring link (subplots b in purple) with different core sizes r_c. Vertical dashed bars are the time t_1 when circulation transfer is 50% complete. Lines depicted as dotted, dashed and solid indicate progressive grid refinement.

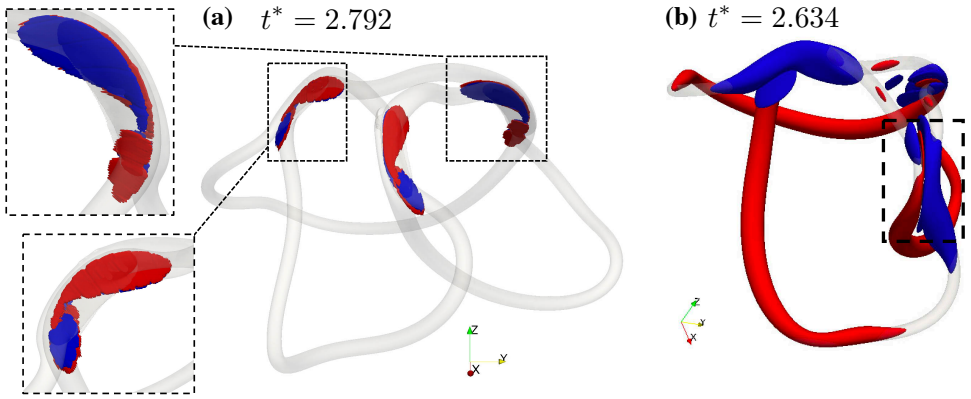

Figure 36: Iso-surface of vorticity magnitude $\omega = 34.17\Gamma/\bar{R}^2$ for the trefoil knot shown as transparent grey: (a) colored isosurfaces of super-helicity $-s\bar{R}^5/\Gamma^2 = \pm 8210$; (b) colored isosurfaces of helicity density $h\bar{R}^3/\Gamma^2 = \pm 9.6$. Red and blue are for positive and negative values, respectively.

structure is not necessarily symmetrical, depending on the evolution of particular vortex structure. The asymmetry of the helicity structure determines the resulting change in helicity in reconnection events, as the theoretical model indicates, the local helicity content carried by the anti-parallel structure is annihilated rapidly during reconnection.

The four-element mechanistic model described in the previous section also indicates that in a reconnection event, the helicity change, or super-helicity, is concentrated at the the position of 'bridge', which is the spot where the vortex filaments switch to the direction transverse to the anti-parallel vortex tubes. This can be visualized by a volumetric-filtered iso-surface of super-helicity (Figure 34) for the trefoil knotted vortex case. With the correlation Eq. 8 indicated by the four-element mechanistic model, the magnitude of helicity 'jump' through the reconnection event can be inferred. Eq. 8 is suggesting that the annihilated helicity is the amount of helicity carried by the pre-reconnection anti-parallel structure. Figure 9 shows the inference of helicity 'jump' magnitude for a two-ring link case and a trefoil knot case, indicating the model provides a decent estimate on this magnitude of helicity change.

Note this explanation does not account for the turbulent cascade reconnections at higher Reynolds numbers, with successive secondary reconnections and spurious small-scale vortex bursting, which will add more complexity to the helicity annihilation process. Figure 37 in fact shows that the synchronization process between the circulation transfer and the helicity ramp is disturbed by fluctuations for the trefoil case with r_c=2 mm at the higher Re Re_Γ=6,000. Nevertheless, as shown by the results in this paper, the suggested model provides a robust explanation for global dynamics of helicity change through the unknotting/unlinking events.

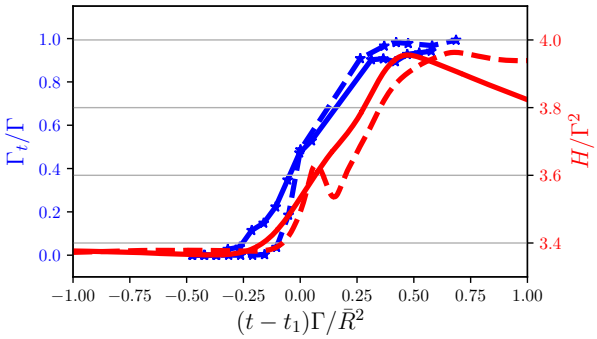

Figure 37: The progression of the circulation transfer (blue) and helicity change (red) of trefoil knot with r_c = 2 mm at Re_Γ=2,000 (—) and 6,000 (– –). t_1 is the time Γ_t/Γ=0.5 for each case.

Challenges

The first major challenge is that even with adaptive mesh refinement, the highest Reynolds number attainable by DNS is still limited. For example, in the DNS attempt to simulate the evolution of the trefoil knotted vortex, the highest Reynolds number resolved with affordable computational cost (i.e. less than 3 million CPU-hours) is only about Re_Γ = 6000, which is considered as an intermediate Reynolds number case. Whereas vortex reconnections will exhibit fully turbulent features (called fully cascade reconnection) when Re_Γ is greater than ≈10000. This challenge is given by the fact that the simulation of topological vortex dynamics resolves from the largest coherent scale to the smallest Kolmogorov scale. Although AMR manages to spend computational resources more efficiently on the finest scales, still the cost of all scales increases exponentially with increased Reynolds number.

This challenge can be targeted with two approaches: first is to seek for the combination of the best of both worlds: LES and AMR-DNS, which are the two major accomplishment in this work. The subgrid scale model of LES approach has its scale-dependence nature, which can be leveraged to its best with the help of AMR. An AMR-LES framework can be engineered to target more complicated flow problem at even higher Reynolds number, and such a model could be formulated with both physics-based and data-based approach. The second approach is to optimize the CFD code to be much more efficient in large-scale super-computing environments, utilizing the latest fruits from Computer Science, including CPU programming, hybrid OpenMP-MPI programming, etc.

The second major challenge is that the understanding on the fundamental physics of the vortex and helicity dynamics in complicated vortex flows is still lacking. This includes the hand-shaking between classic theories – including stability theory, helicity conservation and conversion theory – with complicated vortex flows in practical situations, where vortex structures break down and transition to turbulence under non-linear instability, or interact in a complex vortex system and with solid wall and discontinuities (shock, material interfaces, etc). In the following section, some of the future directions will be inspired by this challenge.

Future Outlook

Stability Study of Trailing Vortices

The advances made through the development of AMR capabilities in the VAMPIRE code allow for a sweeping array of areas to be studied. One of which is the study of the stability, and breakdown dynamics, of trailing vortices. Leveraging the AMR capabilities of VAMPIRE, the CFA Lab has already begun studying the turbulent characteristics of theses vortices. With targeted mesh refinement primary and secondary instabilities can be resolved. This work also delves into the area of topological fluid mechanics to build upon previous work in the area of helicity dynamics [63]. This line of research has obvious applications in high-traffic take-off and landing zones for military aircraft.

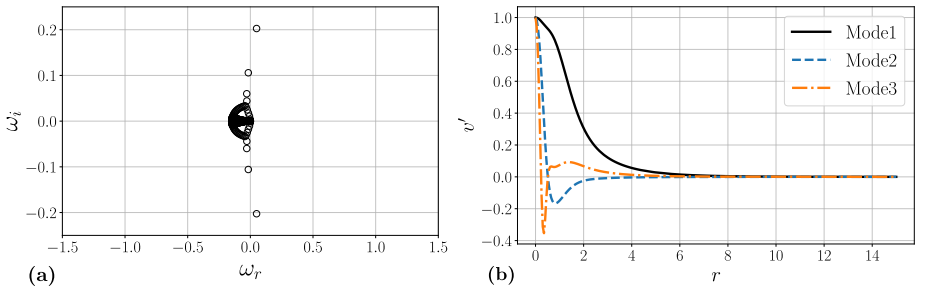

Figure 38: Eigen-spectra and corresponding eigenvectors for the three modal responses with the highest growth rate.

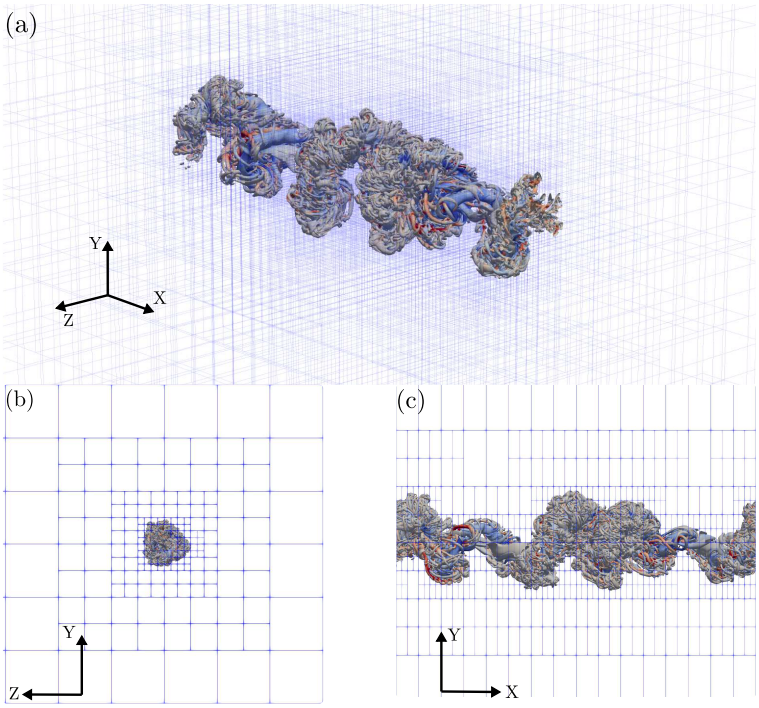

Figure 39: Turbulent breakdown of topologically defined trailing vortex.

The study of vortices from a topological perspective allows for greater levels of abstraction. By describing the geometry of structures within vorticies – and hence turubulent structures – one can calculate and observe the temporal evolution of global quantities. For instance, from a geometric perspective, helicity, $\mathcal{H}$, is the sum of writhe, and twist. The writhe affecting most obviously the shape and possible auto-inductance of the vortex, where the twist is not-so-intuitively directly correlated to the axial velocity. An open question in this field is to relate some topological quantity to Reynolds stresses and the overall stability of the vortex. To answer this question a combination of numerical linear stability and DNS calculations using VAMPIRE will be used.

Explicit Filtering and Extension of CvP-LES

In the other branch of research, development of novel LES methods for high Reynolds number flows, detailed and careful numerical advances are underway. In particular the addition of explicit-filtering capabilities in combination with the CvP-LES technology developed by Chapelier [4]. Explicit-filtering allows for the user to refine the mesh while still maintaining control over the spectral content of the solution. Figure 40 illustrates the how the family of filters adopted damp wavenumbers beyond a desired range. The filters commute with all other derivative and interpolation operators up to a desired order of accuracy. Further development of these filters will involve casting the filters into Padé pseudo-spectral operators.

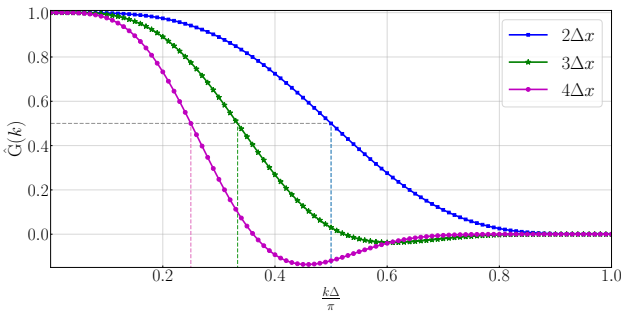

Figure 40: The transfer function of three different filters used to implement the explicitly-filtered Navier-Stokes equations.

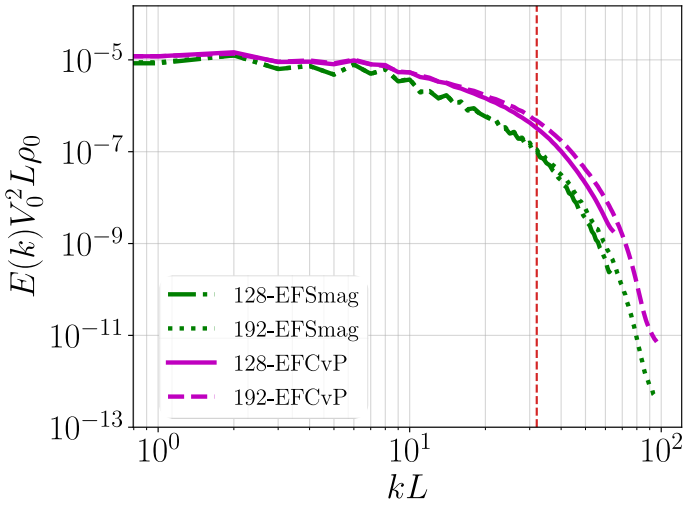

Figure 41: Spectral content of explicitly-filtered LES of a Taylor-Green Vortex at a timestep with a wide range of active length-scales.

The implementation of explicit-filtering allows for great control over the range of spectral content along with a "cleaning" of the solution. Where error would normally accumulate in the high-wavenumber range due to aliasing error, explicit-filtering removes this error from the spectral range of interest to the researcher. Figure 41 illustrates two key concepts. The first is the clear downturn of spectral content of the solution after it has reached the cutoff wavenumber – depicted in Figure 41 as the vertical red line. The second is the advantage that the CvP-LES method gives. Especially clear is the gap between the classic Smagorinsky model and the CvP-LES correction at high-wavenumbers. This difference occurs at a critical time when energy is being transferred from the large to small scales. The CvP correction allows this energy transfer without the erroneous addition of SGS dissipation.

Furthermore, next steps for the evolution of the CvP-LES method – developed under this grant – include an extension to consider the effects of compressible flow. This new technology, when implemented in trans/supersonic flows could even be used for shock capturing.

The Team

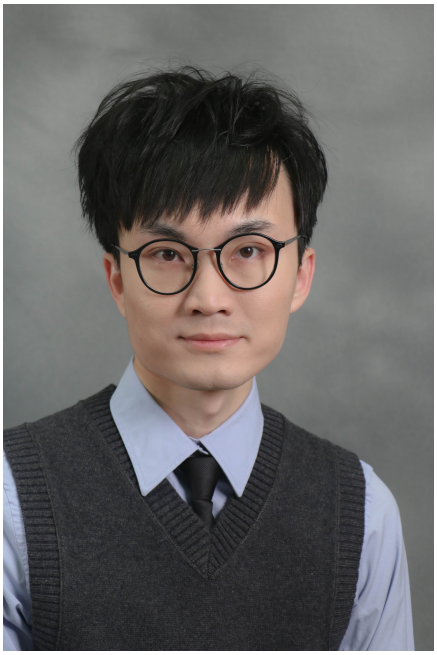

Xinran Zhao is currently a postdoc fellow at the School of Aeronautics and Astronautics at Purdue University. Zhao's research in Fluid Dynamics and Energy Systems relies on high-performance computing and multi-fidelity multi-domain modeling, targeting theoretical and applied fluid flow problems and related engineering designs. Zhao obtained his Ph.D. degree in Mechanical Engineering from Purdue in December 2018, Zhao's Master's degree in Mechanical Engineering from Carnegie Mellon University, and my BS degree in Mechanical Engineering from Shanghai Jiao Tong University, China. In his research experience in graduate schools and postdoctoral appointment, Zhao participated in very diverse research projects and kept expanding his skill set and research portfolio. The research topics that he has engaged in or has interest in include (but not limited to): computational fluid dynamics, vortex dynamics and topological fluid dynamics [62, 63, 69], multi-physics and multi-domain simulation and modeling of fluid machinery and thermo-fulid systems (for example [60, 61, 64–68]).

Jean-Baptiste Chapelier is a research engineer at ONERA (Paris, France) since 2018, in the department of aerodynamics, aeroacoustics and aeroelasticity (DAAA), where he contributes to the development of novel CFD platforms used in the aeronautic industry. He obtained his PhD in 2013 from ONERA/University of Bordeaux with Dr. Rémi Abgrall and Dr. Eric Lamballais as doctoral advisors, then completed two postdoctoral appointments, the first at CORIA/INSA de Rouen, advised by Dr. Guido Lodato (2016) and the second at Purdue/School of Mechanical Engineering, advised by Dr. Carlo Scalo (2018). His expertise is the development of high-order discontinuous finite element methods for the computation of turbulent flows by the means of LES and DNS techniques. He developed in particular multiscale and dynamic models leveraging polynomial scale representation for such numerical methods. His contributions have been published in renowned journals such as Journal of Computational Physics and Computer Methods in Applied Mechanics and Engineering [1–4, 7].

Nicola Lucarelli is currently a Ph.D. student in Dr. Carlo Scalo's Compressible Flow and Acoustics laboratory within the Mechanical Engineering department at Purdue University. His current research is two-pronged with the first branch focusing on vortex stability through the use of high-fidelity numerics on AMR grids in Navier-Stokes codes accompanied by linear stability analysis [34]; the second branch is based on the advancement of large-eddy simulations and subgrid-scale models via the implementation of accurate, grid-independent numerics and low-cost SGS sensors in both incompressible and compressible flows [33]. Lucarelli received his Master's and Bachelor's degrees from Youngstown State Univsersity in December, 2019 and May, 2017, respectively. Here, he researched applied vortex dynamics with the use of RANS turbulence models and image based experimental methods [32]. Along with these topics Lucarelli's research interests also include compressible vortex dynamics, turbulence interactions, shock-vortex interactions, and topological fluid dynamics.

Carlo Scalo is an Associate Professor in the School of Mechanical, and Aeronautical and Astronautical Engineering (by courtesy) at Purdue University. Scalo completed his postdoctoral appointment (2014) at Stanford University working on theoretical and numerical modelling of thermoacoustic instability and sound-turbulence interactions in compressible boundary layers [31, 46, 47]. Prior to that, he obtained his Ph.D. (2012) from Queen's University, Canada, working on subgrid-scale modeling of high-Schmidt-number turbulent mass transfer in equilibrium and non-equilibrium geophysical flows [30, 45, 48–50]. He obtained his B.Eng. (2006) and M.Sc. (2008) degrees in Aeronautical and Astronautical Engineering at the Universita' degli Studi di Napoli - Federico II, Italy. Scalo's research interests focus on computational aeroacoustics [13,18,19,21,22,39,43,55], vortex dynamics [5, 6, 38, 70], low- and high-speed turbulent boundary layers [26, 59], and hypersonics [8,9,54]. Scalo has received three distinct Young Investigator Program (YIP) Awards from the Department of Defense in: hypersonic boundary layer transition (Air Force), hypersonic boundary layer turbulence (Navy) and vortex dynamics (Army). Scalo is also the founder of HySonic Technologies – a Purdue start-up that received several SBIR grants from the US Navy for the design of the new generation of hypersonic vehicles.

References

[1] J-B Chapelier, M de la Llave Plata, F Renac, and E Lamballais. Evaluation of a high-order discontinuous galerkin method for the DNS of turbulent flows. *Comput. Fluids*, 95:210–226, 2014.

[2] J-B Chapelier, G Lodato, and A Jameson. A study on the numerical dissipation of the spectral difference method for freely decaying and wall-bounded turbulence. *Comput. Fluids*, 139:261–280, 2016.

[3] J-B Chapelier and Guido Lodato. A spectral-element dynamic model for the large-eddy simulation of turbulent flows. *J. Comput. Phys.*, 321:279–302, 2016.

[4] J-B Chapelier, B Wasistho, and C Scalo. A coherent vorticity preserving eddy-viscosity correction for large-eddy simulation. *Journal of Computational Physics*, 359:164–182, 2018.

[5] J.-B. Chapelier, B. Wasistho, and C. Scalo. A coherent vorticity preserving eddy-viscosity correction for large-eddy simulation. *Journal of Computational Physics*, 359:164 – 182, 2018.

[6] J.-B. Chapelier, B. Wasistho, and C. Scalo. Large-eddy simulation of temporally developing double helical vortices. *Journal of Fluid Mechanics*, 863:79–113, 2019.

[7] Jean-Baptiste Chapelier, Carlo Scalo, and Bono Wasistho. *Development of adaptive subgrid scale models based on a large-scale vorticity sensor*. American Institute of Aeronautics and Astronautics, 2017/07/29 2017.

[8] Yongkai Chen and Carlo Scalo. Effects of porous walls on near-wall supersonic turbulence. *Phys. Rev. Fluids*, 6:084607, Aug 2021.

[9] Yongkai Chen and Carlo Scalo. Trapped waves in supersonic and hypersonic turbulent channel flow over porous walls. *Journal of Fluid Mechanics*, 920:A24, 2021.

[10] Kelly S Chichak, Stuart J Cantrill, Anthony R Pease, Sheng-Hsien Chiu, Gareth WV Cave, Jerry L Atwood, and J Fraser Stoddart. Molecular borromean rings. *Science*, 304(5675):1308–1312, 2004.

[11] Steven C Crow. Stability theory for a pair of trailing vortices. *AIAA J.*, 8(12):2172–2179, 1970.

[12] Mark R Dennis, Robert P King, Barry Jack, Kevin O'Holleran, and Miles J Padgett. Isolated optical vortex knots. *Nature Physics*, 6(2):118–121, 2010.

[13] Q. Douasbin, C. Scalo, L. Selle, and T. Poinsot. Delayed-time domain impedance boundary conditions (d-tdibc). *Journal of Computational Physics*, 371:50 – 66, 2018.

[14] Maroi Felli, Roberto Camussi, and F Di Felice. Mechanisms of evolution of the propeller wake in the transition and far fields. *J. Fluid Mech.*, 682:5–53, 2011.

[15] M. Germano, U. Piomelli, P. Moin, and W.H. Cabot. A dynamic subgrid-scale eddy viscosity model. *Phys. Fluids*, 3(7):1760–1765, 1991.

[16] Sandip Ghosal, Thomas S Lund, Parviz Moin, and Knut Akselvoll. A dynamic localization model for Large-Eddy simulation of turbulent flows. *J. Fluid Mech.*, 286:229–255, 1995.

[17] BP Gupta and RG Loewy. Theoretical analysis of the aerodynamic stability of multiple, interdigitated helical vortices. *AIAA J.*, 12(10):1381–1387, 1974.

[18] Prateek Gupta, Guido Lodato, and Carlo Scalo. Spectral energy cascade in thermoacoustic shock waves. *Journal of Fluid Mechanics*, 831:358–393, 2017.

[19] Prateek Gupta and Carlo Scalo. Spectral energy cascade and decay in nonlinear acoustic waves. *Phys. Rev. E*, 98:033117, Sep 2018.

[20] Dongran Han, Suchetan Pal, Yan Liu, and Hao Yan. Folding and cutting dna into reconfigurable topological nanostructures. *Nature nanotechnology*, 5(10):712–717, 2010.

[21] Haitian Hao, Carlo Scalo, and Fabio Semperlotti. Axial-mode solid-state thermoacoustic instability: An analytical parametric study. *Journal of Sound and Vibration*, 470:115159, 2020.

[22] Haitian Hao, Carlo Scalo, Mihir Sen, and Fabio Semperlotti. Thermoacoustics of solids: A pathway to solid state engines and refrigerators. *Journal of Applied Physics*, 123(2):024903, 2018.

[23] J. Jiménez, A. A. Wray, P. G. Saffman, and R. S. Rogallo. The structure of intense vorticity in isotropic turbulence. *J. Fluid Mech.*, 255:65–90, 1993.

[24] Hridesh Kedia, Dustin Kleckner, Martin W Scheeler, and William TM Irvine. Helicity in superfluids: Existence and the classical limit. *Physical Review Fluids*, 3(10):104702, 2018.

[25] R.M. Kerr. Higher-order derivative correlations and the alignment of small-scale structures in isotropic numerical turbulence. *J. Fluid Mech.*, 153:31–58, 1985.

[26] Kukjin Kim, Jean-Pierre Hickey, and Carlo Scalo. Pseudophase change effects in turbulent channel flow under transcritical temperature conditions. *Journal of Fluid Mechanics*, 871:52–91, 2019.

[27] Dustin Kleckner and William TM Irvine. Creation and dynamics of knotted vortices. *Nature physics*, 9(4):253–258, 2013.

[28] A.N. Kolmogorov. The local structure of turbulence in incompressible viscous fluid for very large Reynolds numbers. *Dokl. Akad. Nauk SSSR*, 30(4):299–303, 1941.

[29] Eric Lamballais, Olivier Métais, and Marcel Lesieur. Spectral-dynamic model for Large-Eddy simulations of turbulent rotating channel flow. *Theo. Comput. Fluid Dyn.*, 12(3):149–177, 1998.

[30] Geoffrey Lee, Carlo Scalo, and Ugo Piomelli. A simple technique for the visualisation of eddy kinematics in turbulent flows. *International Journal of Computational Fluid Dynamics*, 26(4):263–274, 2012.

[31] Jeffrey Lin, Carlo Scalo, and Lambertus Hesselink. High-fidelity simulation of a standing-wave thermoacoustic–piezoelectric engine. *Journal of Fluid Mechanics*, 808:19–60, 2016.

[32] Nicola Lucarelli, Elise Eckman, and Kevin J Disotell. Cfd analysis of cyclone separator flow field in advance of experiment. In *AIAA Aviation 2019 Forum*, page 3496, 2019.

[33] Nicola M Lucarelli, Jean-Baptiste Chapelier, Bono Wasistho, and Carlo Scalo. Development of an explicitly filtered large-eddy simulation framework for the coherent-vorticity preserving (cvp) eddy viscosity correction. In *AIAA AVIATION 2021 FORUM*, page 2748, 2021.

[34] Nicola M Lucarelli, Xinran Zhao, Robert Morton, William Irvine, and Carlo Scalo. Numerical investigation of the stability of straight twisted vortices. In *AIAA AVIATION 2021 FORUM*, page 2935, 2021.

[35] Peter MacNeice, Kevin M Olson, Clark Mobarry, Rosalinda De Fainchtein, and Charles Packer. Paramesh: A parallel adaptive mesh refinement community toolkit. *Computer physics communications*, 126(3):330–354, 2000.

[36] Charles Meneveau, Thomas S Lund, and William H Cabot. A lagrangian dynamic subgrid-scale model of turbulence. *J. Fluid Mech.*, 319:353–385, 1996.

[37] O. Metais and M. Lesieur. Spectral Large-Eddy Simulation of isotropic and stably stratified turbulence. *J. Fluid Mech.*, 239(1):157–194, 1992.

[38] M. T. Migliorino and C. Scalo. Heat-induced planar shock waves in supercritical fluids. *Shock Waves*, 30(2):153–167, 2020.

[39] Mario Tindaro Migliorino and Carlo Scalo. Real-fluid effects on standing-wave thermoacoustic instability. *Journal of Fluid Mechanics*, 883:A23, 2020.

[40] H Keith Moffatt. Helicity—invariant even in a viscous fluid. *Science*, 357(6350):448–449, 2017.

[41] András Nemes, David Lo Jacono, Hugh M Blackburn, and John Sheridan. Mutual inductance of two helical vortices. *J. Fluid Mech.*, 774:298–310, 2015.

[42] Noma Park, Sungwon Lee, Jungil Lee, and Haecheon Choi. A dynamic subgrid-scale eddy viscosity model with a global model coefficient. *Phys. Fluids*, 18(12):125109, 2006.

[43] Iman Rahbari and Carlo Scalo. Linear stability analysis of compressible channel flow over porous walls. In *Whither Turbulence and Big Data in the 21st Century?*, pages 451–467. Springer International Publishing, August 2017. Rahbari I., Scalo C. (2017) Linear Stability Analysis of Compressible Channel Flow over Porous Walls. In: Pollard

A., Castillo L., Danaila L., Glauser M. (eds) Whither Turbulence and Big Data in the 21st Century?. Springer, Cham.

[44] Hayder Salman. Helicity conservation and twisted seifert surfaces for superfluid vortices. *Proceedings of the Royal Society A: Mathematical, Physical and Engineering Sciences*, 473(2200):20160853, 2017.

[45] C. Scalo, L. Boegman, and U. Piomelli. Large-eddy simulation and low-order modeling of sediment-oxygen uptake in a transitional oscillatory flow. *Journal of Geophysical Research: Oceans*, 118(4):1926–1939, 2013.

[46] Carlo Scalo, Julien Bodart, and Sanjiva K. Lele. Compressible turbulent channel flow with impedance boundary conditions. *Physics of Fluids*, 27(3):035107, 2015.

[47] Carlo Scalo, Sanjiva K. Lele, and Lambertus Hesselink. Linear and nonlinear modelling of a theoretical travelling-wave thermoacoustic heat engine. *Journal of Fluid Mechanics*, 766:368–404, 2015.

[48] Carlo Scalo, Ugo Piomelli, and Leon Boegman. High-schmidt-number mass transport mechanisms from a turbulent flow to absorbing sediments. *Physics of Fluids*, 24(8):085103, 2012.

[49] Carlo Scalo, Ugo Piomelli, and Leon Boegman. Large-eddy simulation of oxygen transfer to organic sediment beds. *Journal of Geophysical Research: Oceans*, 117(C6), 2012.

[50] Carlo Scalo, Ugo Piomelli, and Leon Boegman. Self-similar decay and mixing of a high-schmidt-number passive scalar in an oscillating boundary layer in the intermittently turbulent regime. *Journal of Fluid Mechanics*, 726:338–370, 2013.

[51] Martin W. Scheeler, Dustin Kleckner, Davide Proment, Gordon L. Kindlmann, and William T. M. Irvine. Helicity conservation by flow across scales in reconnecting vortex links and knots. *Proc. Natl. Acad. Sci.*, 111(43):15350–15355, 2014.

[52] Zhen-Su She, Eric Jackson, and Steven A Orszag. Intermittent vortex structures in homogeneous isotropic turbulence. *Nature*, 344(6263):226, 1990.

[53] J. Smagorinsky. General circulation experiments with the primitive equations. *Mon. Weather Rev.*, 91(3):99–164, 1963.

[54] Victor C. B. Sousa, Danish Patel, J.-B. Chapelier, Viola Wartemann, Alexander Wagner, and Carlo Scalo. Numerical investigation of second-mode attenuation over carbon/carbon porous surfaces. *Journal of Spacecraft and Rockets*, 56(2):319–332, 2019.

[55] Shubham Thirani, Prateek Gupta, and Carlo Scalo. Knudsen number effects on the nonlinear acoustic spectral energy cascade. *Phys. Rev. E*, 101:023101, Feb 2020.

[56] Uroš Tkalec, Miha Ravnik, Simon Čopar, Slobodan Žumer, and Igor Muševič. Reconfigurable knots and links in chiral nematic colloids. *Science*, 333(6038):62–65, 2011.

[57] A Vincent and M Meneguzzi. The spatial structure and statistical properties of homogeneous turbulence. *J. Fluid Mech.*, 225:1–20, 1991.

[58] AW Vreman. An eddy-viscosity subgrid-scale model for turbulent shear flow: Algebraic theory and applications. *Phys. Fluids*, 16(10):3670–3681, 2004.

[59] Matthew X. Yao, Zeping Sun, Carlo Scalo, and Jean-Pierre Hickey. Vortical and thermal interfacial layers in wall-bounded turbulent flows under transcritical conditions. *Phys. Rev. Fluids*, 4:084604, Aug 2019.

[60] Xinran Zhao, Akshay Iyer, Patcharapit Promoppatum, and Shi-Chune Yao. Numerical modeling of the thermal behavior and residual stress in the direct metal laser sintering process of titanium alloy products. *Additive Manufacturing*, 14:126–136, 2017.

[61] Xinran Zhao and Mehrdad Massoudi. Flow of granular materials with slip boundary condition: A continuum–kinetic theory approach. *Applied Mathematics and Computation*, 242:518–527, 2014.

[62] Xinran Zhao and Carlo Scalo. *A Compact-Finite-Difference-Based Numerical Framework for Adaptive-Grid-Refinement Simulations of Vortex-Dominated Flows.*

[63] Xinran Zhao and Carlo Scalo. Helicity dynamics in reconnection events of topologically complex vortex flows. *Journal of Fluid Mechanics*, 920, 2021.

[64] Xinran Zhao and Andrea Vacca. Formulation and optimization of involute spur gear in external gear pump. *Mechanism and Machine Theory*, 117:114–132, 2017.

[65] Xinran Zhao and Andrea Vacca. Numerical analysis of theoretical flow in external gear machines. *Mechanism and Machine Theory*, 108:41–56, 2017.

[66] Xinran Zhao and Andrea Vacca. Analysis of continuous-contact helical gear pumps through numerical modeling and experimental validation. *Mechanical Systems and Signal Processing*, 109:352–378, 2018.

[67] Xinran Zhao and Andrea Vacca. Theoretical investigation into the ripple source of external gear pumps. *Energies*, 12(3):535, 2019.

[68] Xinran Zhao and Andrea Vacca. Multi-domain simulation and dynamic analysis of the 3d loading and micromotion of continuous-contact helical gear pumps. *Mechanical Systems and Signal Processing*, 163:108116, 2022.

[69] Xinran Zhao, Zongxin Yu, Jean-Baptiste Chapelier, and Carlo Scalo. Direct numerical and large-eddy simulation of trefoil knotted vortices. *Journal of Fluid Mechanics*, 910, 2021.

[70] Xinran Zhao, Zongxin Yu, Jean-Baptiste Chapelier, and Carlo Scalo. Direct numerical and large-eddy simulation of trefoil knotted vortices. *Journal of Fluid Mechanics*, 910:A31, 2021.